International Communications in Heat and Mass Transfer 157 (2024) 107719

Contents lists available at ScienceDirect

International Communications in Heat and Mass Transfer

journal homepage: www.elsevier.com/locate/ichmt

Vibrational convection in thermal systems: Nano-encapsulated phase change material in a porous enclosure

Nidhal Ben Khedher [a,b], Hakim S. Sultan Aljibori [c], S.A.M. Mehryan [d,*], Ahmad Hajjar [e], Mohammad Ghalambaz [f,g,*], Mohamed Boujelbene [h], Nasrin B.M. Elbashir [i], Ibrahim Mahariq [j,k,*]

[a] Department of Mechanical Engineering, College of Engineering, University of Ha'il, P.O. Box 2440, Ha'il City, Saudi Arabia
[b] Laboratory of Thermal and Energetic Systems Studies (LESTE) at the National School of Engineering of Monastir, University of Monastir, 50000, Tunisia
[c] College of Engineering, University of Warith Al-Anbiyaa, Karbala 56001, Iraq
[d] Department of Mechanical and Energy Engineering, Shahid Beheshti University, A.C., P.O. Box 16765-1719, Tehran, Iran
[e] Center for Environmental Intelligence and College of Engineering and Computer Science, VinUniversity, Hanoi, Viet Nam
[f] Department of Mathematics, Saveetha School of Engineering, SIMATS, Chennai, India
[g] Laboratory on Convective Heat and Mass Transfer, Tomsk State University, 634050 Tomsk, Russia
[h] Industrial Engineering Department, College of Engineering, University of Ha'il, Ha'il 55476, Saudi Arabia
[i] Department of Mathematics, College of Science and Humanities, Prince Sattam Bin Abdulaziz University, Al Kharj 11942, Saudi Arabia
[j] GUST Engineering and Applied Innovation Research Center (GEAR), Gulf University for Science and Technology, Mishref, Kuwait
[k] Department of Medical Research, China Medical University Hospital, China Medical University, Taichung, Taiwan

ARTICLE INFO

Keywords:
Thermal vibrational convection
NEPCM suspension
Porous enclosure
Local thermal non-equilibrium model

ABSTRACT

Suspensions containing the Nano-encapsulated Phase Change Material (NEPCM) are an innovative type of fluid that combines the advantages of nanofluids with the heat storage capabilities of phase change materials. The focus of this study is to analyze how external vibrations influence the natural convection of an NEPCM suspension inside an enclosure saturated with a porous medium. The enclosure is subjected to periodic vibrations in the vertical direction, and the energy equations of the porous medium are subjected to the application of the local thermal non-equilibrium condition. It is found that among the studied parameters, the Rayleigh number, the interfacial coefficient, and the porosity have the highest impact. Increasing the vibration Rayleigh from 1e6 to 1e7 increases by >3.5 times the Nusselt number in the fluid. Reducing the interfacial heat transfer coefficient from 5000 to 100 decreases the Nusselt amplitude in the solid by 4 times and raises the Nusselt amplitude in the fluid by 7 times. Augmenting the porosity from 0.6 to 0.95 decreases the Nusselt number by 15% in the solid. Altering the properties of the nanoparticles, i.e., their fraction and fusion temperature, also affects heat transfer but to a lesser extent.

1. Introduction

The field of thermal fluid dynamics has seen significant advances in recent years, propelling industries ranging from energy storage to climate control systems. At the intersection of these innovations lies the concept of thermal vibrational convection within porous enclosures, which is essential for optimizing thermal energy transfer.

Heat transfer within enclosures filled by porous media is an increasingly significant subject of inquiry, especially in applications such as thermal storage, electronics cooling, and advanced energy systems [1,2]. The porous medium provides high thermal efficiency while offering various advantages like enhanced thermal conductivity and easier control over heat and mass transport. Several studies investigated the dynamic of convection heat transfer in enclosures filled with a porous medium and saturated by heat transfer fluids, such as water or nanofluids [3,4]. The concept of local thermal non-equilibrium (LTNE) and its relevance to heat transfer in porous medium has undergone thorough analysis [5,6]. The expansion of the LTNE condition is confirmed to correlate with an increase in the Darcy parameter, providing a greater degree of control over heat and mass transfer processes [7]. An intriguing study involves a porous square enclosure filled with a Newtonian fluid [8]. This study presented novel insights into the impact of the LTNE phenomena on heat transfer and entropy generation

* Corresponding authors.
E-mail addresses: alal171366244@gmail.com (S.A.M. Mehryan), m.ghalambaz@gmail.com (M. Ghalambaz), ibmahariq@gmail.com (I. Mahariq).

https://doi.org/10.1016/j.icheatmasstransfer.2024.107719

Available online 11 July 2024

Nomenclature

Latin symbols

b^*	Amplitude of sinusoidal vibration (m)
c_p^*	Sensible heat capacity ($Jkg^{-1}K^{-1}$)
Da	Darcy number
g^*	Gravity acceleration (ms^{-2})
H^*	Size of square (m)
h^*	Interfacial heat transfer coefficient ($Wm^{-2}K^{-1}$)
k^*	Thermal conductivity ($Wm^{-1}K^{-1}$)
Nc	Thermal conductivity number
Nu	Nusselt number
Nv	Dynamic viscosity number
p^*	Pressure (Pa)
Pr	Prandtl number
Ra_g	Gravity Rayleigh number
Ra_Ω	Vibration Rayleigh number
Ste	Stefan number
T^*	Temperature (K)
t^*	Time (s)
$\vec{v}^*$	Velocity vector (ms^{-1})
x^*, y^*	Cartesian coordinates (m)

Greek symbols

β^*	Thermal expansion coefficient (K^{-1})
ε	Porosity
ρ^*	Density (kgm^{-3})
κ^*	Permeability (m^{-2})
μ^*	Dynamic viscosity ($kgm^{-1}s^{-1}$)
ξ^*	Wave frequency (s^{-1})
ϕ	Volume fraction of NEPCM
ω	Proportion of weights between core and shell

Subscripts

a	Time average
bf	Base fluid
c	Cold/ core
h	Hot
l	Local value
m	Melting point/ mean value
max	Maximum value
mf	Metal foam
np	Nanoparticle
s	Shell
se	Suspension
t	Total

in thermal-free convection within a non-Darcy porous medium.

Phase change materials (PCMs) possess a notable heat of phase change, allowing them to store and release substantial thermal energy during transitions between solid and liquid states, and vice versa. When encapsulated at the nanoscale, these PCMs can be uniformly distributed within a fluid, creating a suspension of nano-encapsulated phase change material (NEPCM) [9,10]. The growing emphasis on energy-efficient heat transfer systems has spurred interest in NEPCMs, which are often suspended in host fluids like water. These materials are characterized by their ability to absorb and release heat, making them excellent candidates for various engineering applications, especially in confined spaces like enclosures or cavities [11,12]. While traditional fluid systems leverage only sensible heat for energy transfer, NEPCMs add an additional layer of efficiency through latent heat storage in their nanoparticles [13]. The heat transfer characteristics of NEPCMs in enclosures are influenced by a range of operational and geometric factors, encompassing the Rayleigh number, the concentration of the nanoparticles, the melting temperature of the particle core, and the inclination angle of the medium [14].

Introducing such NEPCM suspensions into porous media, characterized by an intricate network of solid obstacles, elevates the complexity and potential applications of thermal vibrational convection phenomena, with the porosity and Darcy number also coming into play [15,16]. Some studies indicate that these factors can exert a significant impact on the rate of heat transfer. For instance, under specific conditions, a modest 5% volume concentration of NEPCMs could result in a notable 20.1% improvement in the heat transfer rate [15]. On the other hand, porous media like nickel foam could significantly improve the cooling efficiency compared to NEPCMs alone [16].

The impact of vibrations on heat transfer in confined spaces such as enclosures or cavities has drawn significant research attention, influencing the flow structures, mass, and heat transfer rates in various geometries under different boundary conditions. The mechanical vibration phenomenon holds relevance to various real-life applications, particularly in fields involving fluid dynamics and structural mechanics. Some potential applications include industrial processes [17], electronic devices [18], aerospace and automotive engineering [19,20], and energy systems [21]. For instance, A study of vertical vibrations applied to horizontal cylinders indicated that when the amplitude-diameter ratio exceeded 0.5, the vibrational heat-transfer coefficient increased linearly regardless of vibration frequency [22]. Besides Mishra et al. [23] conducted a comparative study using a well-validated computational fluid dynamics model to study the impacts of vibration on heat transfer. They found that as the frequency levels increased, the significance of vibrations decreased, but alterations in amplitude became more influential. Under conditions of vibrational flow, a significant enhancement of about 540% compared to that in a steady-state flow scenario was observed.

In horizontally-enclosed concentric and eccentric annular cylinders, the impact of vertical mechanical vibrations on heat transfer rates is pronounced, particularly when combined with changes in the Rayleigh number [24]. The data showed that a rise in the Rayleigh number corresponded to a nearly proportional increase in the average Nusselt number. High-frequency horizontal vibrations applied to a shallow cavity with thermally insulating walls demonstrated a stabilizing effect on buoyant convection [25]. Conversely, in a cubic enclosure subjected to vertical vibrations, the influence varied with the Rayleigh number [26]. While high Rayleigh numbers saw gravitational thermal convection prevail, making vibrations less effective, lower numbers experienced a significant boost in heat transfer rates due to vibrations. Computational studies on a square enclosure revealed irregular variations in the average Nusselt number with the angular frequency of vibration, indicating the unpredictable nature of vibrational thermal convection [27]. Additionally, experiments on horizontal cylinders containing fluids such as H_2O, engine oil and kerosene showed that vibrations led to a linear increase in the local heat transfer coefficient, with the Nusselt number increasing consistently from the bottom to the top of the cylinder [28].

Research on partially porous cavities subjected to vertical vibration demonstrated that such vibration decreased flow intensity and penetration into the porous section [29]. This phenomenon, in turn, resulted in lower heat and mass transfer rates, which could be beneficial in applications where limited permeability and temperature gradients are required. Studies on vertical fin arrays corroborated the idea that vibrations could substantially enhance heat transfer rates beyond a certain threshold value of amplitude and frequency [30].

Previous studies have explored various aspects of free convection heat transfer of NEPCM suspensions under normal conditions without significant vibrational effects. However, mechanical vibrations can

Table 1
The thermophysical specifications of the used substances, as referenced in [33–35].

Material	μ (kg/m.s)	β (K^{-1})	C_p (J/Kg.K)	k (W/m.K)	ρ (kg/m^3)
Host fluid	8.9×10^{-4}	21×10^{-5}	4179	0.613	997.1
Polyurethane	NA*	17.28×10^{-5}	1317.7	0.025	786
Nonadecane	3.49×10^{-3}	8×10^{-4}	2037	0.260	721
Solid matrix	NA	NA	897	205	2700

* Not applicable

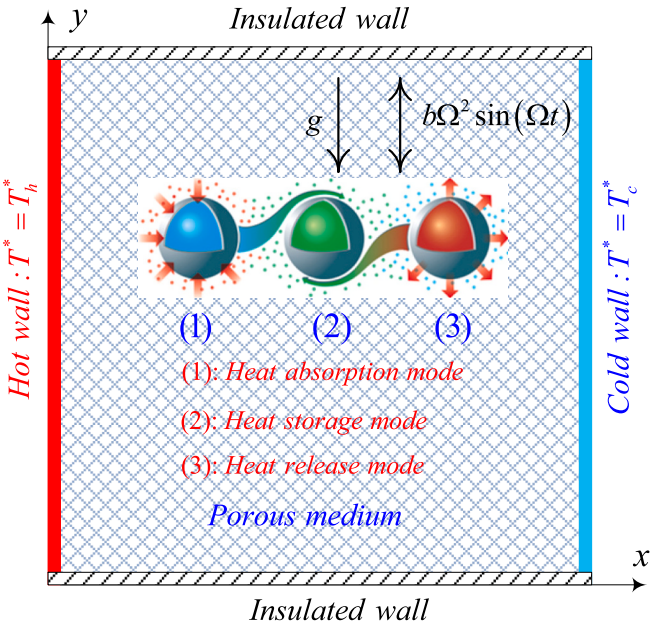

Fig. 1. Schematic configuration.

significantly alter the flow patterns of free convection and heat transfer within enclosures. These vibrations can arise from intentional or unintentional movement of device components. Despite their importance, the interaction between mechanical vibrations and the heat transfer properties of these advanced nanomaterials within enclosures remains unexplored. The novelty of the present study can be summarized as follows:

- Examination of the thermo-vibrational behavior of a fluid within a porous medium.
- Exploration of the influence of vibrational convection on the heat and flow patterns of a NEPCM suspension.
- Analysis of the effects of thermo-vibrational convection on the heat transfer rate inside a porous enclosure containing the NEPCM suspension.

2. Physics of the issue and modeling approach

2.1. Physics of the issue

An enclosed square cavity with a dimension of H^* is considered, where the medium filling the cavity is porous. The pores within the porous foam are filled with a blend of aqueous solution and nano-sized particles of NEPCM. The particles consist of nonadecane and polyurethane as their respective core and shell ingredients. Table 1 provides an overview of the characteristics associated with the components comprising both the solid matrix and the suspension. Fig. 1 provides a visual depiction of the schematic representation of the capsule configuration being studied. The cavity is subjected to a vertical gravitational modulation in a sinusoidal pattern, indicating periodic fluctuations in the gravitational force along the vertical direction. A local thermal non-equilibrium (LTNE) temperature difference between the porous matrix and the fluid inside the pores was considered [31,32]. The sinusoidal vibrations occurring within the cavity are characterized by their amplitude, indicated by b^*, and frequency, denoted by Ω^*. Hence, the instantaneous gravitational acceleration, $g_v^*(t^*)$, can be expressed as the sum of a fixed term g^*, and a time-dependent component, $b^*\Omega^{*2}sin(\Omega^* t^*)$. It is noteworthy that $\Omega^* = 2\pi\xi^*$. The walls on the left and right, referred to as the active walls, maintain the temperatures of T_h^* and T_c^*, respectively. The boundaries aligned with the horizon are regarded as adiabatic, implying that no heat transfer takes place across these walls. The analysis is based on several key assumptions:

1- The suspension is assumed to follow Newton's law of viscosity, making it a Newtonian suspension.

2- The motion is assumed to be in two dimensions, occurring within a single plane for simplicity.

3- Laminar flow is presumed in this study, characterized by smooth and predictable motion without turbulence.

4- The amplitude of the vibration velocity is assumed to be relatively small to maintain linearity in the system.

5- The fluid is considered incompressible, ensuring that the fluid density remains constant throughout the analysis.

6- With the exclusion of density in the source of the momentum equation, the suspension's characteristics are presumed to remain constant throughout the analysis.

7- The validity of the Boussinesq approximation is assumed and confirmed for the analysis. This approximation is widely accepted for scenarios where the fluid density variations are relatively small compared to the mean density and can be neglected, except in the buoyancy term of the governing equations. By making this assumption, the analysis becomes more feasible and computationally efficient while still capturing the essential physics of the problem accurately.

9- The porous system utilizes aluminum foam as the solid matrix material. The local thermal non-equilibrium (LTNE) condition holds between the suspension and metal foam.

10- Given that the driving force of fluid flow is solely buoyancy forces, fluid velocities are quite small, rendering drag forces negligible. As a result, the fluid flow was modeled using the Darcy flow model.

These assumptions form the foundation for the analysis, allowing us to focus on specific aspects of the problem while maintaining a reasonable level of accuracy and tractability.

Under the assumptions mentioned earlier, the governing equations for the problem can be written in dimensional form as follows [14,36,37]:

Continuity equation (Balance of Mass):

$$\nabla^* . \vec{\boldsymbol{v}}^* = 0 \tag{1}$$

Navier-Stokes equation (Balance of Linear Momentum):

$$\frac{\rho_{se}^*}{\varepsilon}\frac{\partial \vec{\boldsymbol{v}}^*}{\partial t^*} + \frac{\rho_{se}^*}{\varepsilon^2}\vec{\boldsymbol{v}}^* . \nabla^* \vec{\boldsymbol{v}}^* = -\nabla^* p^* + \frac{\mu_{se}^*}{\varepsilon}\nabla^{*2}\vec{\boldsymbol{v}}^* - \frac{\mu_{se}^*}{\kappa^*}\vec{\boldsymbol{v}}^* + \left(g^* + b^*\Omega^{*2} sin(\Omega^* t^*)\right)\rho_{se}^*\beta_{se}^*\left(T_{se}^* - T_c^*\right)\vec{\boldsymbol{j}} \tag{2}$$

Here, Ω^* is considered as $2\pi\xi^*$ where ξ^* is the wave frequency. ρ_{se}^* is the fluid density, t^* is time, $\vec{\boldsymbol{v}}^*$ is the velocity vector, ∇^* is the gradient

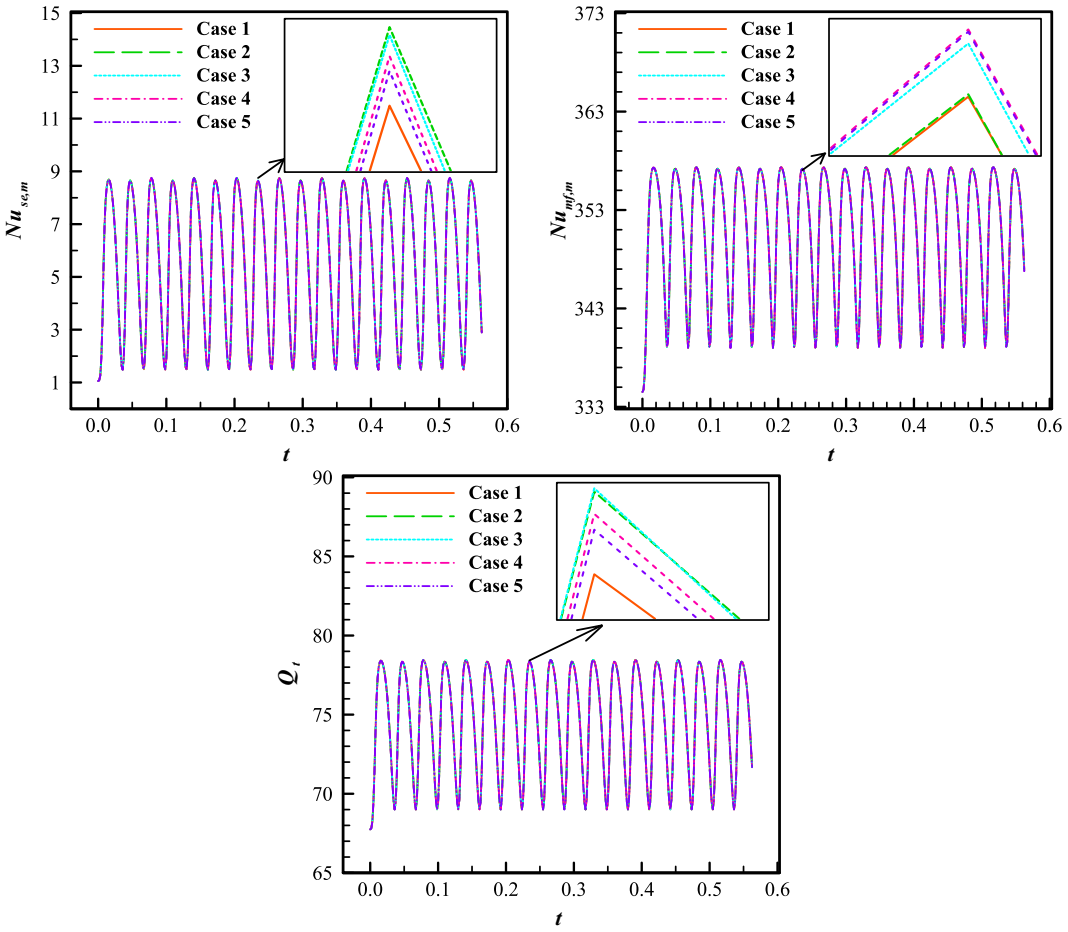

Fig. 2. Variations of $Nu_{se,m}$, $Nu_{mf,m}$, and Q_t for the mesh with different numbers of elements.

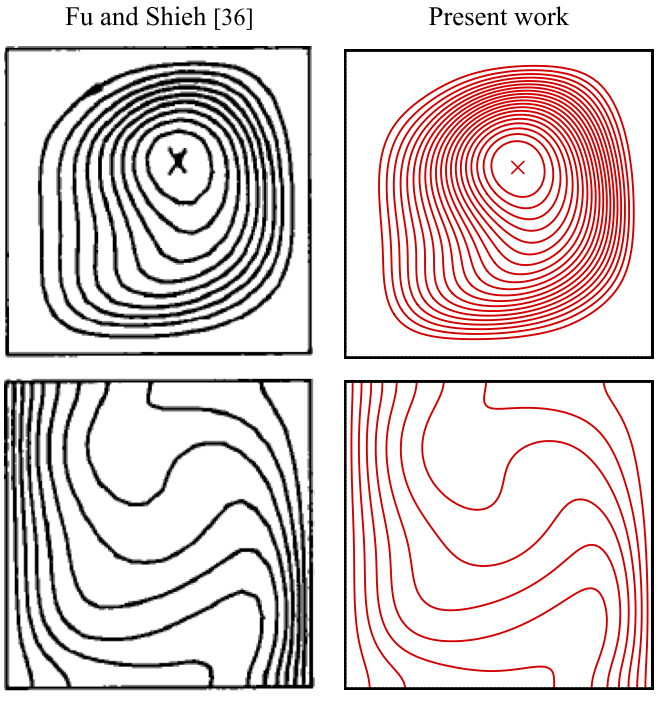

Fig. 3. Comparison between the isotherms and streamlines presented in [36] (with permission from Elsevier) and those predicted in the present study for $Ra_g = 10^4$, $Ra_\Omega = 1.41 \times 10^5$, $\Omega = 100$, and $Pr = 0.71$.

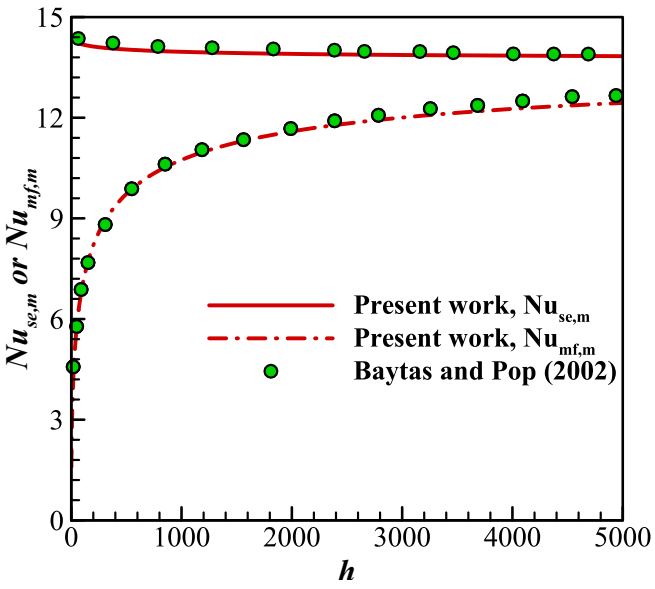

Fig. 4. Comparison between the mean Nusselt numbers of suspension and metal foam presented in [39] and those predicted in the present study for different values of h parameter when $Ra_g \times Da = 10^3$, $Ra_\Omega = \Omega = \phi = 0.0$, and $k_{mf}/k_{bf} = 10$

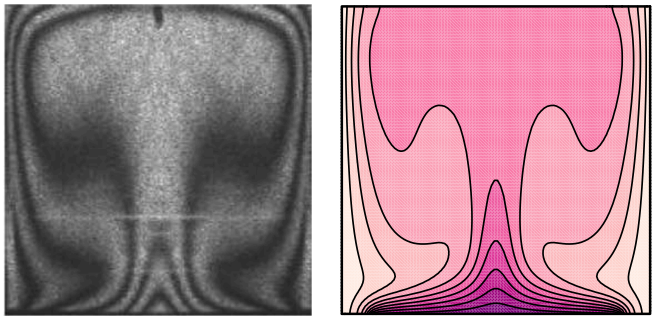

Fig. 5. (a) The isotherms obtained from the experimental-based work [40] (with permission from Elsevier), and (b) the isotherms simulated by the current work under the conditions where the dimensionless heat source length is 0.8, $Ra_g = 1.836 \times 10^5$, and $Pr = 0.71$,

Table 2
Comparison between the average Nusselt numbers reported in [41,42] and those obtained in the present work; $Ste = 0.313$, $Ra_g = 10^5$.

T_m	Ref. [41]	Ref. [42]	Present work
0.1	4.9550	4.9551	4.9554
0.2	5.1022	5.1022	5.1023
0.3	5.1932	5.1932	5.1931

operator, p^* is the pressure, μ^*_{se} is the dynamic viscosity of the fluid, g^* is the gravity acceleration, b^* is the amplitude of oscillation, β^*_{se} is the thermal expansion coefficient of the suspension, ε is the porosity of the medium, κ^* is the permeability.

Energy equation (Balance of Energy) [38]:

$$\varepsilon\rho^*_{se}c^*_{p,se}\frac{\partial T^*_{se}}{\partial t^*}+\rho^*_{se}c^*_{p,se}\vec{\boldsymbol{v}}^*.\nabla^*T^*_{se}=\varepsilon k^*_{se}\nabla^{*2}T^*_{se}+h^*\left(T^*_{mf}-T^*_{se}\right) \tag{3}$$

where T^*_{se} is the temperature of the suspension, T^*_{mf} is the temperature of the solid matrix, $c^*_{p,se}$ is the specific heat capacity at constant pressure, k^*_{se} is the thermal conductivity of the suspension, and h^* is the coefficient of convective heat transfer between the suspension and the solid matrix [38].

$$(1-\varepsilon)\rho^*_{mf}c^*_{p,mf}\frac{\partial T^*_{mf}}{\partial t}=(1-\varepsilon)k^*_{mf}\nabla^{*2}T^*_{mf}-h^*\left(T^*_{mf}-T^*_{se}\right) \tag{4}$$

ρ^*_{mf} is the density of the solid matrix, $c^*_{p,mf}$ is the sensible heat capacity of the solid matrix, and k^*_{mf} is the thermal conductivity of the solid matrix. These equations, along with appropriate boundary conditions, constitute the set of governing equations for the problem at hand, taking into account the specified assumptions and physical properties of the fluid. Regarding the physical characteristics of the situation, the boundary conditions can be articulated in the following manner:

$$0\le y^*\le H^*, x^*=0, x^*=H^*:\vec{\boldsymbol{v}}^*=0, T^*_{se}=T^*_{mf}=T^*_h \tag{5-a}$$

$$0\le x^*\le H^*, y^*=0, H^*:\vec{\boldsymbol{v}}^*=0, \frac{\partial T^*_{se}}{\partial y^*}=\frac{\partial T^*_{mf}}{\partial y^*}=0 \tag{5-b}$$

Furthermore, the initial state or condition is:

$$0\le x^*\le H^*, 0\le y^*\le H^*:\vec{\boldsymbol{v}}^*=0, T^*_{se}=T^*_{mf}=0 \tag{5-c}$$

2.2. Thermal and physical characteristics of the suspension

The density of the mixture is [38]:

$$\rho^*_{se}=\phi\rho^*_{np}-\phi\rho^*_{bf}+\rho^*_{bf} \tag{6}$$

in which, ρ^*_{bf} is the density of the base fluid, ϕ the volume fraction of the nano-sized particles of NEPCM dispersed in the host liquid, and ρ^*_{np} the density of the nano-sized particles of NEPCM is calculated as the following [38]:

$$\rho^*_{np}=\frac{(1+\omega^{-1})\rho^*_s\rho^*_c}{\left(\omega^{-1}\rho^*_s+\rho^*_c\right)} \tag{7}$$

ρ^*_s is the shell density of the nano-sized particles of NEPCM, and ρ^*_c is the core density of the nano-sized particles of NEPCM. ω is the proportion of weights between the core and shell components and stands at roughly 0.447. $c^*_{p,se}$ as the specific heat capacity of the mixture is [38]:

$$c^*_{p,se}=\phi\left(\frac{\rho^*_{np}}{\rho^*_{se}}\right)c^*_{p,np,eff}-\phi\left(\frac{\rho^*_{bf}}{\rho^*_{se}}\right)c^*_{p,bf}+\left(\frac{\rho^*_{bf}}{\rho^*_{se}}\right)c^*_{p,bf} \tag{8}$$

The effective heat capacity of the nano-sized particles, denoted by $c^*_{p,np,eff}$, is as follows [38]:

$$c^*_{p,np,eff}=\left\{\frac{\pi}{2}\times\left(\frac{L^*_{sf}}{\Delta^*T^*}-c^*_{p,na}\right)\times sin\left(\pi\left(\frac{1}{2}+\frac{T^*-T^*_m}{\Delta^*T^*}\right)\right)\right\}Y^*+c^*_{p,na} \tag{9-a}$$

$$Y^*=\begin{cases}0 & T^*<-(\Delta^*T^*\Delta^*T^*22)+T^*_m\\ 0 & T^*>0.5\times\Delta^*T^*+T^*_m\\ 1 & -0.5\times\Delta^*T^*+T^*_m<T^*<0.5\times\Delta^*T^*+T^*_m\end{cases} \tag{9-b}$$

The coefficient of thermal-volume expansion of the mixture is defined as follows [38]:

$$\beta^*_{se}=\beta^*_{bf}+\phi\left(\beta^*_{np}-\beta^*_{bf}\right) \tag{10}$$

Thermal conductivity of the mixture is defined as the following [38]:

$$k^*_{se}=k^*_{bf}(1+Nc\times\phi) \tag{11}$$

The dynamic viscosity of the mixture is [38]:

$$\mu^*_{se}=\mu^*_{bf}(1+Nv\times\phi) \tag{12}$$

Nc is the thermal conductivity number, and Nv is the dynamic viscosity number.

2.3. Deriving dimensionless formulation for governing equations

The transformation of the governing equations from dimensional coordinates to dimensionless ones involves the use of the following set of dimensionless variables:

$$\vec{v}^*=\frac{\rho^*_{bf}c^*_{p,bf}H^*}{k^*_{bf}}\vec{v}^*, p=\frac{\rho^*_{bf}c^{*2}_{p,bf}H^{*2}}{k^{*2}_{bf}}p^*, T_{se}=\frac{T^*_{se}-T^*_c}{T^*_h-T^*_c}, T_{mf}=\frac{T^*_{mf}-T^*_c}{T^*_h-T^*_c}$$
$$, \nabla=\frac{\nabla^*}{L^*}, \xi=\frac{\rho^*_{bf}c^*_{p,bf}H^{*2}}{k^*_{bf}}\xi^*, (x,y)=\frac{(x^*,y^*)}{H^*}, t=\frac{k^*_{bf}}{\rho^*_{bf}c^*_{p,bf}H^{*2}}t^* \tag{13}$$

Utilizing the normalization parameters stated above, the equations are transformed into their normalized counterparts:

$$\nabla.\vec{\boldsymbol{v}}=0 \tag{14}$$

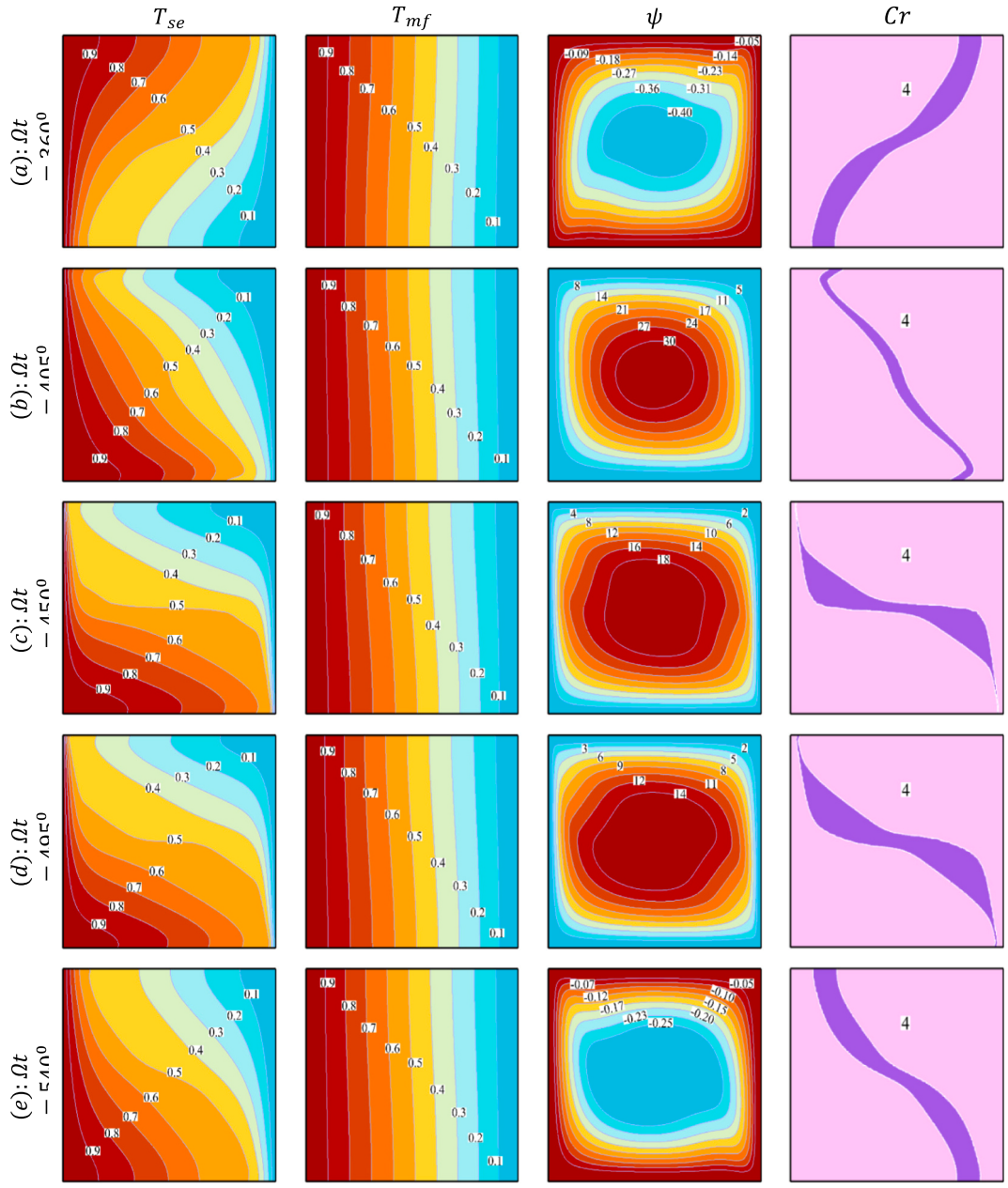

Fig. 7. T_{se}, T_{mf}, ψ, and Cr for the second cycle at (a) $t = 0.0641$, (b) $t = 0.0719$, (c) $t = 0.0797$, (d) $t = 0.0875$, (e) $t = 0.0953$, (f) $t = 0.1031$, (g) $t = 0.1109$, (h) $t = 0.1188$, and (i) $t = 0.1266$.

T_{se}, T_{mf}, ψ, and Cr for the second cycle at (a) $t = 0.0641$, (b) $t = 0.0719$, (c) $t = 0.0797$, (d) $t = 0.0875$, (e) $t = 0.0953$, (f) $t = 0.1031$, (g) $t = 0.1109$, (h) $t = 0.1188$, and (i) $t = 0.1266$.

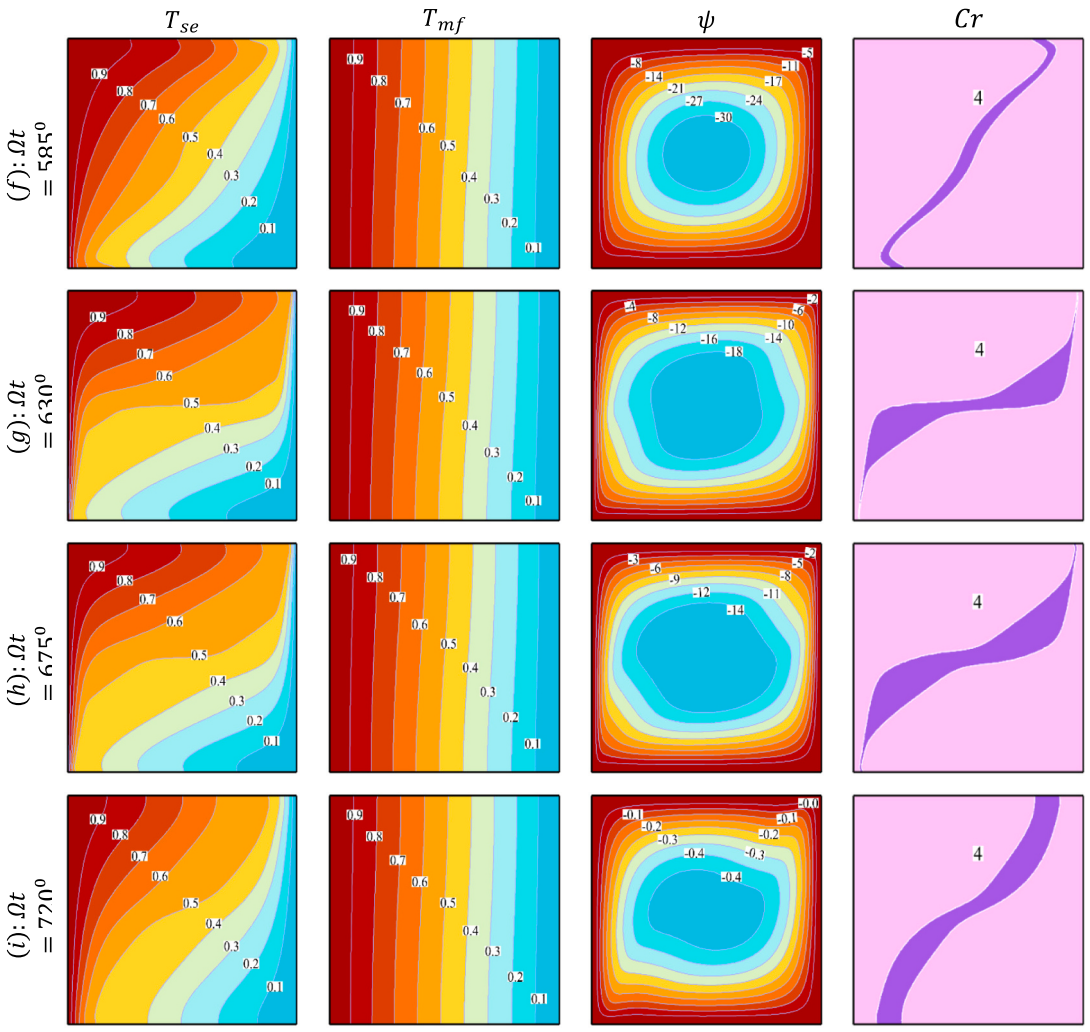

Fig. 7. (*continued*).

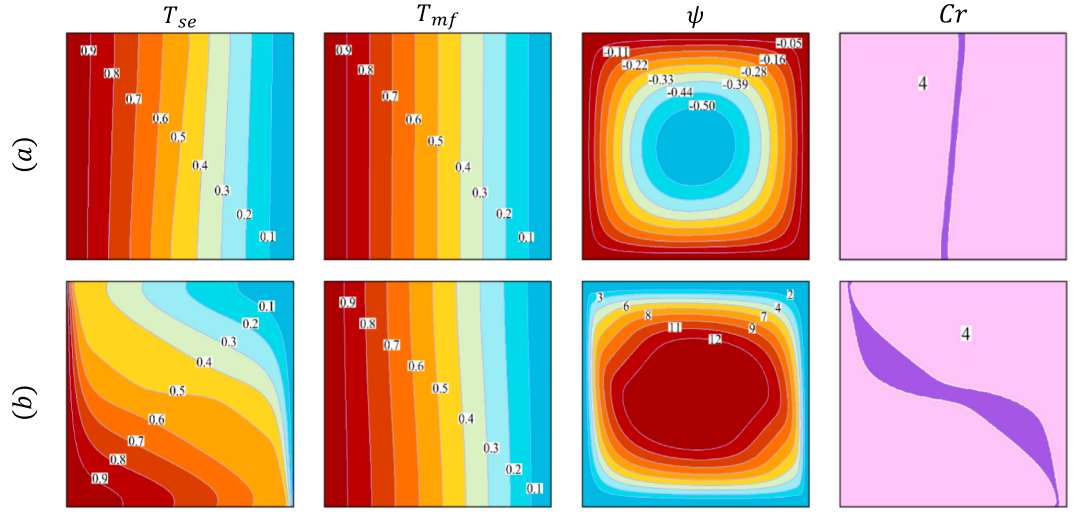

Fig. 8. T_{se}, T_{mf}, ψ, and Cr for (a) $Ra_{\Omega} = 10^4$, and (b) $Ra_{\Omega} = 10^7$ at $t = 0.0572$ ($\Omega t = 540^{o}$)

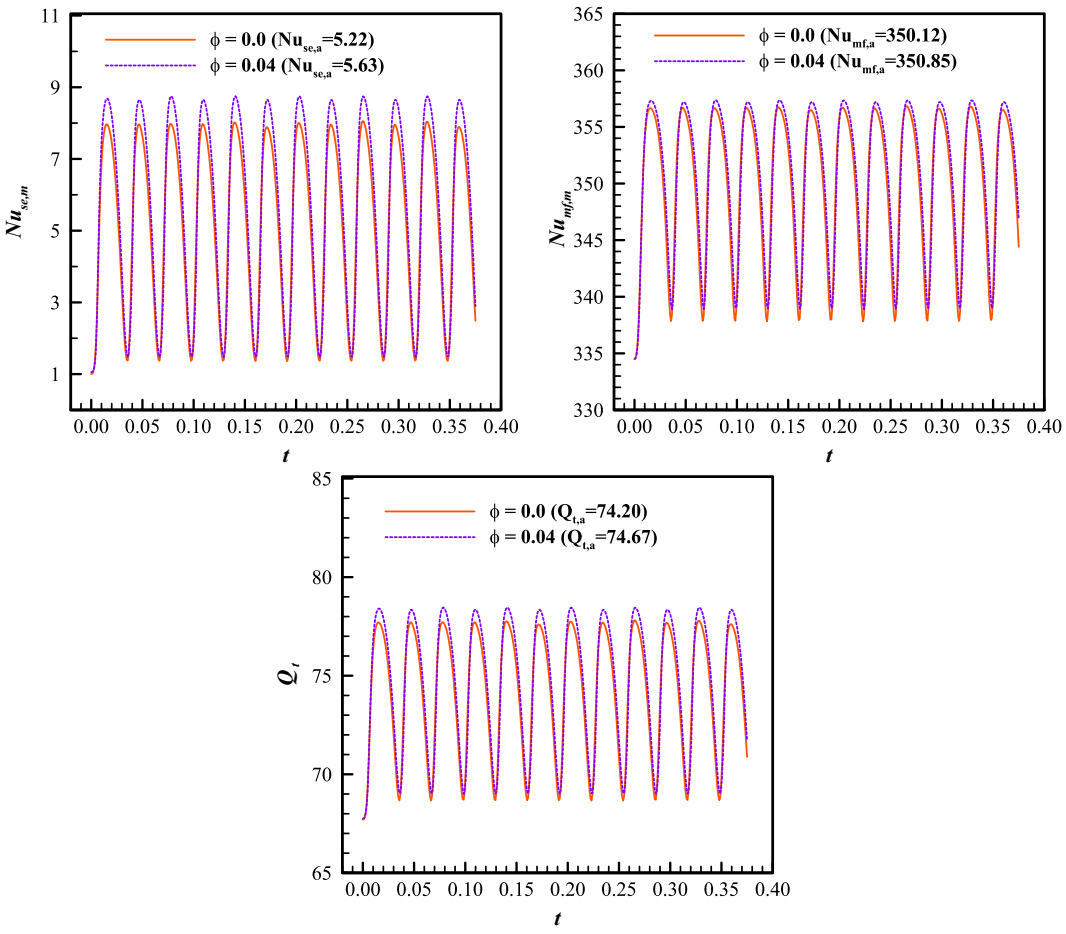

Fig. 9. $Nu_{se,m}$, $Nu_{mf,m}$, and Q_t over the time for $\phi = 0.0$ and $\phi = 0.04$

$$\left(1-\phi+\phi\left(\frac{\rho^*_{np}}{\rho^*_{bf}}\right)\right)\left(\frac{1}{\varepsilon}\frac{\partial\vec{\boldsymbol{v}}}{\partial t}+\frac{1}{\varepsilon^2}\vec{\boldsymbol{v}}.\nabla\vec{\boldsymbol{v}}\right)=-\nabla p+\frac{Pr}{\varepsilon}(1+N\boldsymbol{v}\times\phi)\nabla^2\vec{\boldsymbol{v}}$$
$$+Ra_gPr\begin{pmatrix}(1-\phi)^2+(1-\phi)\phi\left(\frac{\rho^*_{np}}{\rho^*_{bf}}\right)\\+(1-\phi)\phi\left(\frac{\beta^*_{np}}{\beta^*_{bf}}\right)+\phi^2\left(\frac{\rho^*_{np}}{\rho^*_{bf}}\right)\left(\frac{\beta^*_{np}}{\beta^*_{bf}}\right)\end{pmatrix}T\vec{\boldsymbol{j}}-\frac{Pr}{Da}(1+N\boldsymbol{v}\times\phi)\vec{v}$$
$$+Ra_\Omega Pr\begin{pmatrix}(1-\phi)^2+(1-\phi)\phi\left(\frac{\rho^*_{np}}{\rho^*_{bf}}\right)\\+(1-\phi)\phi\left(\frac{\beta^*_{np}}{\beta^*_{bf}}\right)+\phi^2\left(\frac{\rho^*_{np}}{\rho^*_{bf}}\right)\left(\frac{\beta^*_{np}}{\beta^*_{bf}}\right)\end{pmatrix}Tsin(\Omega t)\vec{\boldsymbol{j}} \tag{15}$$

where $\Omega = 2\pi\xi$. Moreover, Pr is Prandtl number, Ra_g gravity Rayleigh number, Ra_Ω vibration Rayleigh number, and Da Darcy number:

$$Pr=\frac{\mu^*_{bf}}{\rho^*_{bf}\alpha^*_{bf}}, Ra_g=\frac{g^*\rho^*_{bf}\beta^*_{bf}\left(T^*_h-T^*_c\right)H^{*3}}{\alpha^*_{bf}\mu^*_{bf}}, Ra_\Omega$$
$$=\frac{b^*\Omega^{*2}\rho^*_{bf}\beta^*_{bf}\left(T^*_h-T^*_c\right)H^{*3}}{\alpha^*_{bf}\mu^*_{bf}}, Da=\frac{\kappa^*}{H^{*2}} \tag{16}$$

$$Cr\varepsilon\left(\frac{\partial T_{se}}{\partial t}+\vec{\boldsymbol{v}}.\nabla T_{se}\right)=\varepsilon(1+Nc\times\phi)\nabla^2T_{se}+h\left(T_{mf}-T_{se}\right) \tag{17}$$

in which

$$Cr=\frac{\rho^*_{se}c^*_{p,se}}{\rho^*_{bf}c^*_{p,bf}}=1-\phi+\phi\lambda+\phi\frac{f}{\Delta TSte} \tag{18-a}$$

where

$$\lambda=\frac{\left(\rho^*_c\rho^*_sc^*_{p,c}+\rho^*_c\rho^*_s\omega c^*_{p,s}\right)}{\left(\rho^*_{bf}\rho^*_sc^*_{p,bf}+\rho^*_{bf}\rho^*_c\omega c^*_{p,bf}\right)}, \Delta T=\frac{\Delta T^*}{\left(T^*_h-T^*_c\right)}, Ste$$
$$=\frac{\rho^*_{bf}c^*_{p,bf}\left(T^*_h-T^*_c\right)\left(\rho^*_s+\omega\rho^*_c\right)}{L^*_{sf}\rho^*_c\rho^*_s} \tag{18-b}$$

$$f=\frac{\pi}{2}sin\left(\frac{\pi}{\Delta T}(T-T_m+\Delta T/2)\right)\Upsilon \tag{18-c}$$

$$\Upsilon=\begin{cases}0 & T<-0.5\Delta T+T_m\\0 & T>0.5\Delta T+T_m\\1 & -0.5\Delta T+T_m<T<0.5\Delta T+T_m\end{cases} \tag{18-d}$$

$$(1-\varepsilon)\left(\frac{\rho_{mf}}{\rho_{bf}}\right)\left(\frac{c_{p,mf}}{c_{p,bf}}\right)\frac{\partial T_{mf}}{\partial t}=(1-\varepsilon)\left(\frac{k_{mf}}{k_{bf}}\right)\nabla^2T_{mf}-h\left(T_{mf}-T_{se}\right) \tag{19}$$

where

$$h=\frac{H^{*2}}{k^*_{bf}}h^* \tag{20}$$

The boundary conditions that govern the physics of the problem are expressed in a mathematical and dimensionless format as follows:

$$x=0, 0\le y\le 1:\vec{\boldsymbol{v}}=0, T_{se}=T_{mf}=1 \tag{21-a}$$

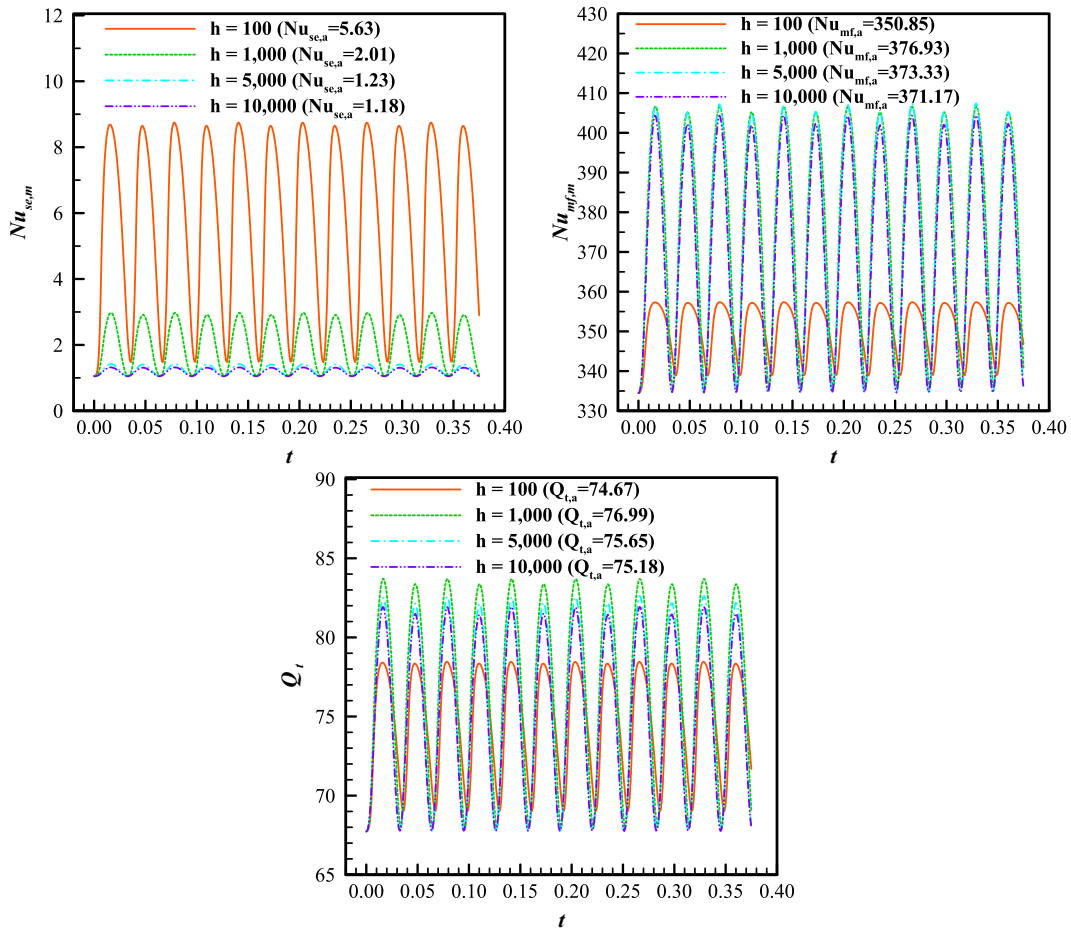

Fig. 10. $Nu_{se,m}$, $Nu_{mf,m}$, and Q_t over time for different values of h

$$x = 1, 0 \le y \le 1 : \vec{\boldsymbol{v}} = 0, T_{se} = T_{mf} = 0 \tag{21-b}$$

$$y = 0, 1, 0 \le x \le 1 : \vec{\boldsymbol{v}} = 0, \frac{\partial T_{se}}{\partial y} = \frac{\partial T_{mf}}{\partial y} = 0 \tag{21-c}$$

Furthermore, the initial condition is:

$$\vec{\boldsymbol{v}} = 0, T_{se} = T_{mf} = 0 \; for \; t = 0, 0 \le y \le 1, 0 \le x \le 1 \tag{21-d}$$

2.4. Heat transfer rate

The relations provided below are employed to calculate the local Nusselt numbers at the heated boundary:

$$Nu_{se,l} = -(1 + Nc \times \phi)\left(\frac{\partial T_{se}}{\partial x}\right)|_{x=0} \tag{22}$$

$$Nu_{mf,l} = -\left(\frac{k_{mf}}{k_{bf}}\right)\left(\frac{\partial T_{s}}{\partial x}\right)|_{x=0} \tag{23}$$

The mean Nusselt number is determined through the integration of the aforementioned equations:

$$Nu_{se,m} = -(1 + Nc \times \phi)\int_0^1 \left(\frac{\partial T_{se}}{\partial x}\right)|_{x=0}\, dy \tag{24}$$

$$Nu_{mf,m} = -\left(\frac{k_{mf}}{k_{bf}}\right)\int_0^1 \left(\frac{\partial T_{mf}}{\partial x}\right)|_{x=0}\, dy \tag{25}$$

The assessment of total heat transfer is also conducted in the following manner:

$$Q_t = \varepsilon \times \left(Nu_{se,m} - Nu_{mf,m}\right) + Nu_{mf,m} \tag{26}$$

The formulation of time-averaged heat transfer rates can subsequently be expressed:

$$Nu_{se,a} = -\frac{(1 + Nc \times \phi)}{t_{\max}}\int_0^{t_{\max}}\int_0^1 \left(\frac{\partial T_{se}}{\partial x}\right)|_{x=0}\, dydt \tag{27}$$

$$Nu_{mf,a} = \frac{-1}{t_{\max}}\left(\frac{k_{mf}}{k_{bf}}\right)\int_0^{\tau_{\max}}\int_0^1 \left(\frac{\partial T_{mf}}{\partial x}\right)|_{x=0}\, dydt \tag{28}$$

$$Q_{t,a} = \frac{1}{t_{\max}}\int_0^{t_{\max}} \left[\varepsilon \times \left(Nu_{se,m} - Nu_{mf,m}\right) + Nu_{mf,m}\right] dt \tag{29}$$

At last, the equation for the stream function is introduced as follows:

$$\frac{\partial^2 \psi}{\partial x^2} + \frac{\partial^2 \psi}{\partial y^2} = \frac{\partial u}{\partial y} - \frac{\partial v}{\partial x} \tag{30}$$

where u and v symbolize the respective components of the velocity vector along the x and y axes.

3. Computational methodology, mesh analysis, and verification

The analysis delves into the implementation of the Galerkin finite element (GFE) approach for solving the dimensionless fundamental equations, considering the prescribed boundary conditions of the

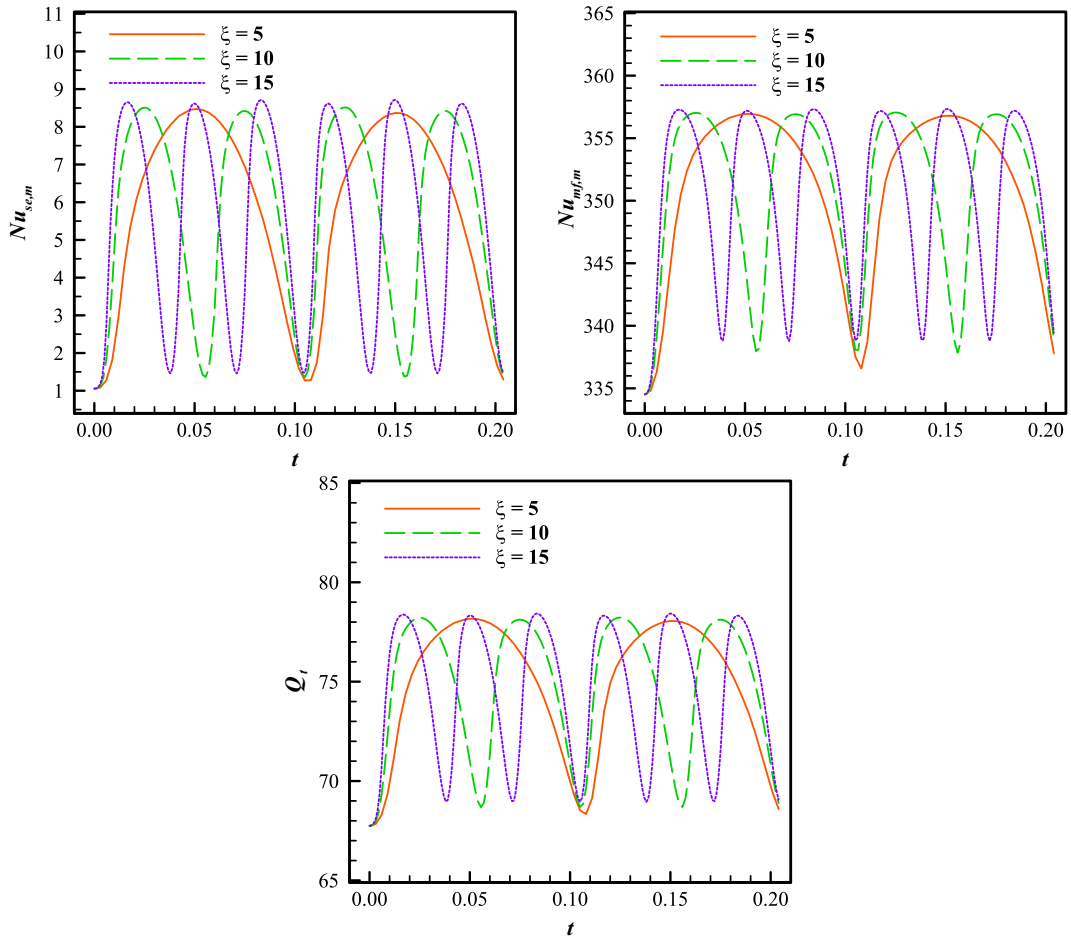

Fig. 11. $Nu_{se,m}$, $Nu_{mf,m}$, and Q_t over the time for $\xi = 5$ ($\Omega = 31.4$), $\xi = 10$ ($\Omega = 62.8$), and $\xi = 15$ ($\Omega = 94.2$)

physical domain [37]. The mass balance equation, acting as a constraint, is employed to determine the pressure variable. For solving Eqs. (14), (15), (17), and (19), the GFE approach is employed, wherein the pressure variable is removed using a sufficiently large expression, denoted as Γ. The fulfillment of the incompressibility conditions as described by Eq. (14), yields:

$$p = -\Gamma \nabla . \vec{\boldsymbol{v}} \tag{31}$$

The continuity equation naturally holds for considerable values of Γ. Replacing the pressure term with this penalty function yields the subsequent equation.

$$\left(1-\phi+\phi\left(\frac{\rho^*_{np}}{\rho^*_{bf}}\right)\right)\left(\frac{1}{\varepsilon}\frac{\partial \vec{\boldsymbol{v}}}{\partial t}+\frac{1}{\varepsilon^2}\vec{\boldsymbol{v}}.\nabla\vec{\boldsymbol{v}}\right)=\nabla(\Gamma\nabla.\vec{\boldsymbol{v}})+\frac{Pr}{\varepsilon}(1+Nv\times\phi)\nabla^2\vec{\boldsymbol{v}}$$
$$+Ra_g Pr\begin{pmatrix}(1-\phi)^2+(1-\phi)\phi\left(\frac{\rho^*_{np}}{\rho^*_{bf}}\right)\\ +(1-\phi)\phi\left(\frac{\beta^*_{np}}{\beta^*_{bf}}\right)+\phi^2\left(\frac{\rho^*_{np}}{\rho^*_{bf}}\right)\left(\frac{\beta^*_{np}}{\beta^*_{bf}}\right)\end{pmatrix}T\vec{\boldsymbol{j}}-\frac{Pr}{Da}(1+Nv\times\phi)\vec{\boldsymbol{v}}$$
$$+Ra_\Omega Pr\begin{pmatrix}(1-\phi)^2+(1-\phi)\phi\left(\frac{\rho^*_{np}}{\rho^*_{bf}}\right)\\ +(1-\phi)\phi\left(\frac{\beta^*_{np}}{\beta^*_{bf}}\right)+\phi^2\left(\frac{\rho^*_{np}}{\rho^*_{bf}}\right)\left(\frac{\beta^*_{np}}{\beta^*_{bf}}\right)\end{pmatrix}Tsin(\Omega t)\vec{\boldsymbol{j}} \tag{32}$$

A set of functions (basis set, $\{\eta_k\}_{k=1}^n$) can be used to represent the velocity components and temperatures of the suspension and metal foam [37].

$$u=\sum_{k=1}^{n}u_k\eta_k(x,y), v=\sum_{k=1}^{n}v_k\eta_k(x,y), T=\sum_{k=1}^{n}T_k\eta_k(x,y) \tag{33}$$

The GFE approach produces nonlinear residual equations at the nodes within the interior domain as follows:

$$R_j^{(1)} \approx A_1 \sum_{k=1}^{n} u_k \int \frac{\partial \eta_k}{\partial t}\eta_j dxdy + A_2 \sum_{k=1}^{n} u_k \int \left(\left(\sum_{k=1}^{n} u_k \eta_k \right) \frac{\partial \eta_k}{\partial x} + \left(\sum_{k=1}^{n} v_k \eta_k \right) \frac{\partial \eta_k}{\partial y} \right) \eta_j dxdy$$
$$+\Gamma \left(\sum_{k=1}^{n} u_k \int \frac{\partial \eta_j}{\partial x}\frac{\partial \eta_k}{\partial x} dxdy + \sum_{k=1}^{n} v_k \int \frac{\partial \eta_j}{\partial x}\frac{\partial \eta_k}{\partial y} dxdy \right) + A_3 \sum_{k=1}^{n} u_k \int \left(\frac{\partial \eta_j}{\partial x}\frac{\partial \eta_k}{\partial x} + \frac{\partial \eta_j}{\partial y}\frac{\partial \eta_k}{\partial y} \right) dxdy \quad (34)$$
$$-A_4 \sum_{k=1}^{n} \int (u_k \eta_k)\eta_j dxdy$$

$$R_j^{(2)} \approx A_1 \sum_{k=1}^{n} v_k \int \frac{\partial \eta_k}{\partial t}\eta_j dxdy + A_2 \sum_{k=1}^{n} v_k \int \left(\left(\sum_{k=1}^{n} u_k \eta_k \right) \frac{\partial \eta_k}{\partial x} + \left(\sum_{k=1}^{n} v_k \eta_k \right) \frac{\partial \eta_k}{\partial y} \right) \eta_j dxdy$$
$$+\Gamma \left(\sum_{k=1}^{n} u_k \int \frac{\partial \eta_j}{\partial y}\frac{\partial \eta_k}{\partial x} dxdy + \sum_{k=1}^{n} v_k \int \frac{\partial \eta_j}{\partial y}\frac{\partial \eta_k}{\partial y} dxdy \right) + A_3 \sum_{k=1}^{n} v_k \int \left(\frac{\partial \eta_j}{\partial x}\frac{\partial \eta_k}{\partial x} + \frac{\partial \eta_j}{\partial y}\frac{\partial \eta_k}{\partial y} \right) dxdy \quad (35)$$
$$-A_4 \sum_{k=1}^{n} \int (v_k \eta_k)\eta_j dxdy + A_5 \int \left(\sum_{k=1}^{n} T_k \eta_k \right) \eta_j dxdy$$

$$R_j^{(3)} \approx \sum_{k=1}^{n} A_6 T_{se,k} \int \frac{\partial \eta_k}{\partial t}\eta_j dxdy + \sum_{k=1}^{n} A_6 T_{se,k} \int \left(\left(\sum_{k=1}^{n} u_k \eta_k \right) \frac{\partial \eta_k}{\partial x} + \left(\sum_{k=1}^{n} v_k \eta_k \right) \frac{\partial \eta_k}{\partial y} \right) \eta_j dxdy$$
$$+A_7 \sum_{k=1}^{n} T_{se,k} \int \left(\frac{\partial \eta_j}{\partial x}\frac{\partial \eta_k}{\partial x} + \frac{\partial \eta_j}{\partial y}\frac{\partial \eta_k}{\partial y} \right) dxdy + h \int \left(\sum_{k=1}^{n} \left(T_{mf,k} - T_{se,k} \right) \eta_k \right) \eta_j dxdy \quad (36)$$

$$R_j^{(4)} \approx A_8 \sum_{k=1}^{n} T_{mf,k} \int \frac{\partial \eta_k}{\partial t}\eta_j dxdy + A_9 \sum_{k=1}^{n} T_{mf,k} \int \left(\frac{\partial \eta_j}{\partial x}\frac{\partial \eta_k}{\partial x} + \frac{\partial \eta_j}{\partial y}\frac{\partial \eta_k}{\partial y} \right) dxdy$$
$$-h \int \left(\sum_{k=1}^{n} \left(T_{mf,k} - T_{se,k} \right) \eta_k \right) \eta_j dxdy \quad (37)$$

where

$$A_1 = \frac{1}{\varepsilon}\left(1 - \phi + \phi\left(\frac{\rho_{np}^*}{\rho_{bf}^*}\right)\right), A_2 = \frac{1}{\varepsilon^2}\left(1 - \phi + \phi\left(\frac{\rho_{np}^*}{\rho_{bf}^*}\right)\right), A_3 = \frac{Pr}{\varepsilon}(1 + Nv \times \phi)$$
$$A_4 = \frac{Pr}{Da}(1 + Nv \times \phi), A_5 = Pr\left(Ra_g + Ra_\Omega sin(\Omega t)\right) \left(\begin{array}{c} (1-\phi)^2 + (1-\phi)\phi\left(\frac{\rho_{np}^*}{\rho_{bf}^*}\right) \\ +(1-\phi)\phi\left(\frac{\beta_{np}^*}{\beta_{bf}^*}\right) + \phi^2\left(\frac{\rho_{np}^*}{\rho_{bf}^*}\right)\left(\frac{\beta_{np}^*}{\beta_{bf}^*}\right) \end{array} \right) \quad (38)$$
$$A_6 = Cr\varepsilon, A_7 = \varepsilon(1 + Nc \times \phi), A_8 = (1-\varepsilon)\left(\frac{\rho_{mf}}{\rho_{bf}}\right)\left(\frac{c_{p,mf}}{c_{p,bf}}\right), A_9 = (1-\varepsilon)\left(\frac{k_{mf}}{k_{bf}}\right)$$

The numerical computations involved integrating using biquadratic functions and a three-point Gaussian quadrature method. Next, the Newton–Raphson method was utilized to determine the coefficients of expansions. The process iteratively solved residual equations until the residual error decreased to 1e-6.

Prior to commencing the numerical solution of Eqs. (14), (15), (17), and (19) with the specified boundary conditions, a preliminary computation is conducted using diverse non-uniform grids comprising square elements: case 1: 75 × 75, case 2: 100 × 100, case3: 125 × 125, case 4: 150 × 150, and case 5: 175 × 175. The objective is to achieve solutions that are independent of the grid used. These experiments demonstrate that the mean Nusselt numbers of the mixture, solid matrix, and the overall heat transfer for 125 × 125 elements exhibit only a marginal disparity compared to the outcomes obtained for higher element counts (Fig. 2). Ultimately, 125 × 125 elements are chosen as a compromise between computational precision and efficiency.

We conducted a thorough accuracy assessment of our numerical model by cross-referencing it with the published numerical solution by Fu and Shieh [36]. This comparison specifically focused on the thermal vibrational convection of air within a square chamber. Fig. 3 shows this evaluation, considering the isothermal and streamlines. The validation shows a remarkable alignment between the streamlines and isothermal contours, illustrating a highly favorable correlation between the results of Fu and Shieh [36] and those predicted by the current work. For the second validation, we compare the Nusselt numbers of the metal foam and mixture phases within a porous enclosure reported in [39] with those obtained in the current investigation. As Fig. 4 depicts, the evaluation is conducted for various values of interfacial heat transfer coefficient, *h*. As evident, a favorable agreement is apparent, affirming the capability of the developed GFE code to accurately simulate the process of convection heat transfer in a porous medium.

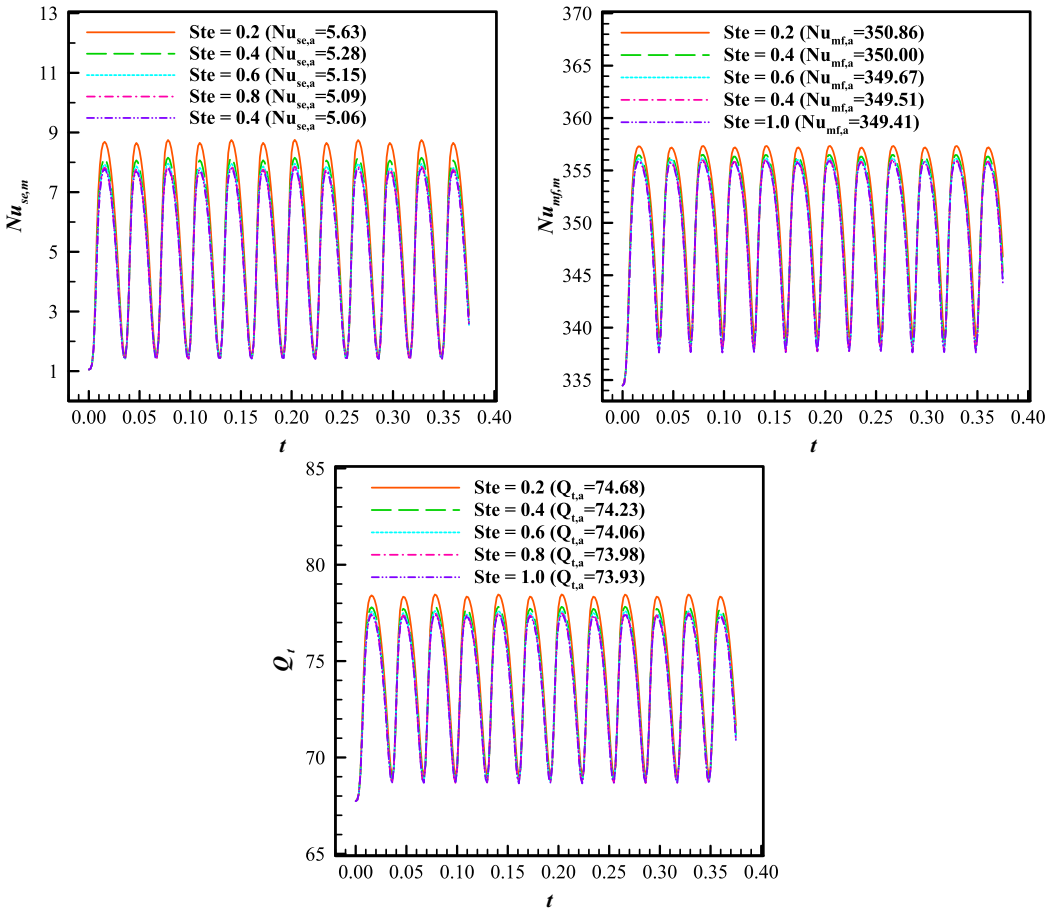

Fig. 12. $Nu_{se,m}$, $Nu_{mf,m}$, and Q_t over time for different values of *Ste*

Fig. 5 visually compares the temperature fields between the experimental work conducted by Calcagni et al. [40] and the current study. In this experiment, the lateral walls are maintained cold while the bottom wall is partially heated. As illustrated, there is a strong agreement between the experimental and numerical results. Furthermore, to validate the model used in simulating the suspension flow containing NEPCM particles, we compare the average Nusselt numbers of the suspension flow within an enclosure under free convection, as reported in [41,42], with those predicted by our current study across various melting points of the core of the NEPCM particles. The outcomes of this assessment are summarized in Table 2. The precise values acquired through the current code affirm the accuracy of our modeling and simulation efforts.

4. Results and discussion

In the present investigation, an array of dimensionless parameters takes center stage, each playing a crucial role in unraveling the dynamics of heat transfer. These include the gravity Rayleigh number, Ra_g, the vibration Rayleigh number, Ra_Ω, the frequency of vibration denoted by ξ ($\Omega = 2\pi\xi$), the Prandtl number, *Pr*, the Stefan number, *Ste*, the concentration of nano-sized particles of NEPCM, ϕ, the melting temperature, T_m, the thermal conductivity number, *Nc*, the dynamic viscosity number, *Nv*, the interfacial heat transfer coefficient, *h*, porosity, ε, and the Darcy number, *Da*. These parameters collectively weave the fabric of our exploration, offering insights into the complex interplay of forces and properties shaping the phenomena under scrutiny. Following the findings reported by Barlak et al. [33], the thermal conductivity of the mixture compared to the host liquid is 1.24 times at $\phi = 0.04$. Additionally, the ratio of dynamic viscosities is 1.5 for the same concentration. The values of both constant and variable parameters are presented in Appendix A.

Fig. 7 illustrates the isothermal contours for the solid matrix (T_{mf}) and the mixture (T_{se}), the streamlines (ψ), and the fields of heat capacity ratio (*Cr*) in the cavity at several instants. First, it can be seen that the isotherms of T_{mf} are almost vertical in all cases. This indicates minimal influence of vibrational impacts on heat transfer through the solid matrix. As for the fluid, its hydrodynamic and thermal behaviors are greatly affected by vibration. In cases (a) and (i), corresponding to the beginning and end of a vibration period, respectively, Ωt equals 360 and 720. At these points, $sin(\Omega t)$ equals 0.0, indicating the absence of vibrational effects. This represents the simple case of a free convection in a cavity differentially heated on its sides. The fluid near the hot wall gets heated, and its density decreases. This hot fluid goes up and gets replaced by a colder fluid due to the buoyancy effects, which results in the free convection clockwise recirculation zone observed in the cavity. The isothermal contours also exhibit characteristics typical of free convection. Hot isotherms ($T_{se} > 0.5$) expand at the top and contract at the bottom, while the opposite trend is observed for colder isotherms. In the presence of vibrational effects, cases (b) to (d) represent the first half period. In these cases, $sin(\Omega t) > 0.0$, so that the cavity is moving downwards. The buoyancy effects are therefore reduced compared to the vibrational ones. This alters the flow patterns, causing the recirculation zone to shift in a counterclockwise direction. Additionally, the flow intensity significantly escalates at the onset of motion and then gradually tapers off until the cavity momentarily halts in case (e), where free convection once again governs the flow behavior. In cases (b) to (d), the isothermal lines track the variations in the flow patterns. The influence of cavity motion supersedes that of free convection, leading to an extension of the cold isothermal zone near the top, while hot isothermal lines expand at the bottom. In case (d), the isotherms appear almost

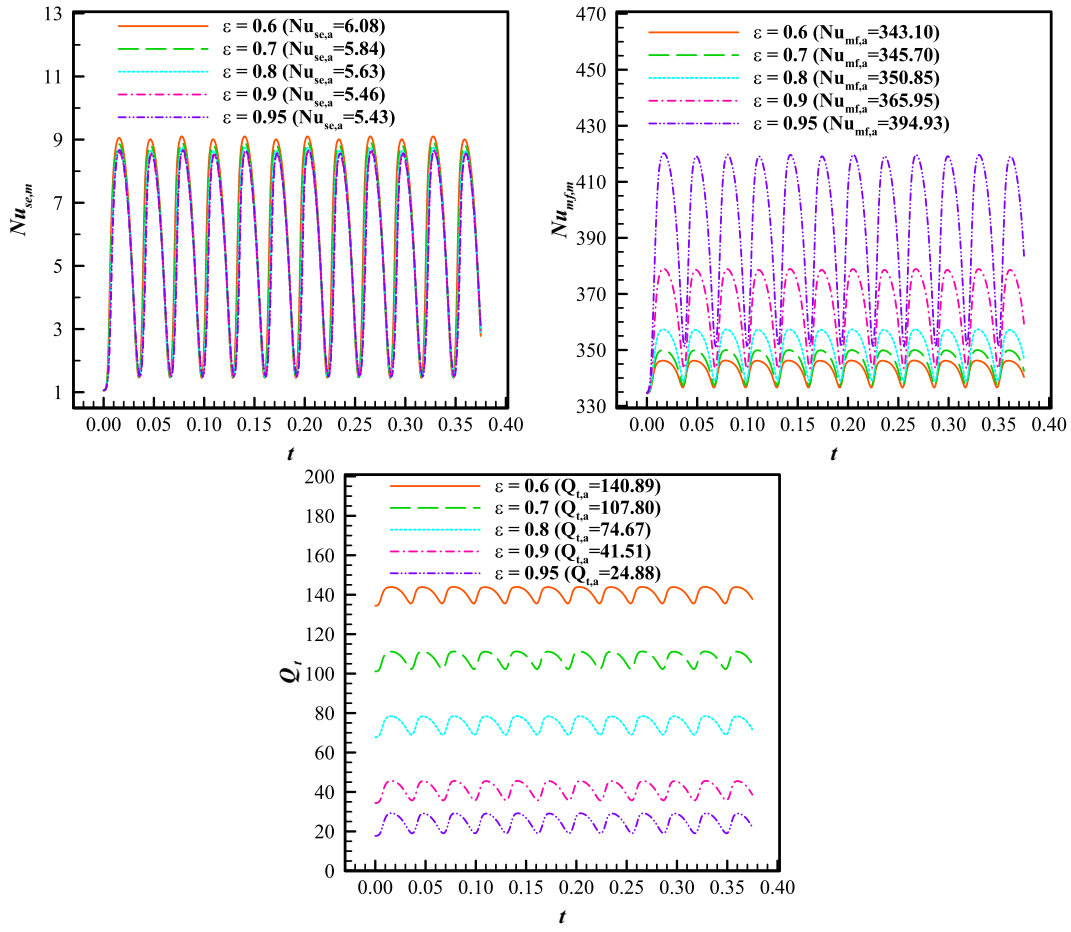

Fig. 13. $Nu_{se,m}$, $Nu_{mf,m}$, and Q_t over time for different values of ε

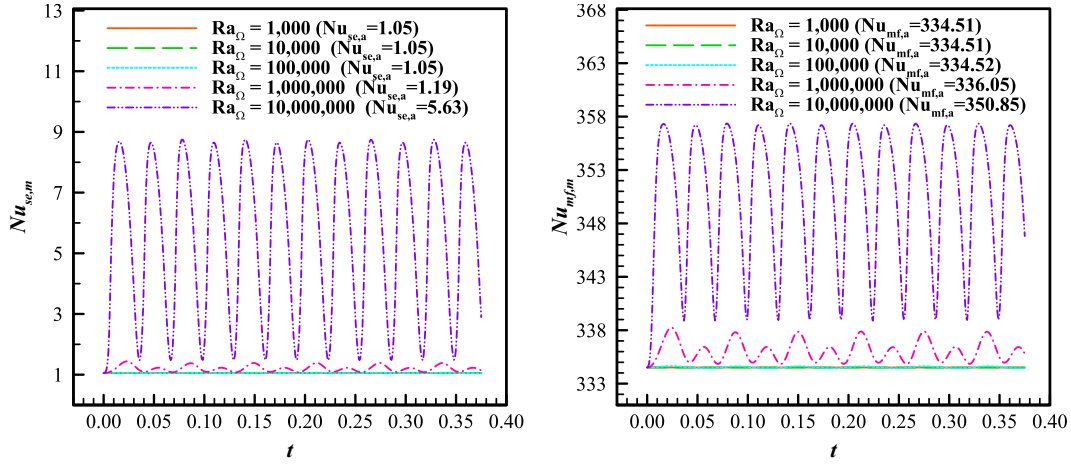

Fig. 14. $Nu_{se,m}$, and $Nu_{mf,m}$ over time for different values of Ra_Ω;($Ra_\Omega = 10^3 : Q_{t,a} = 67.74, Ra_\Omega = 10^4 : Q_{t,a} = 67.74$, $Ra_\Omega = 10^5 : Q_{t,a} = 67.75, Ra_\Omega = 10^6 : Q_{t,a} = 68.16$ and $Ra_\Omega = 10^7 : Q_{t,a} = 74.67$).

horizontal in the middle of the enclosure due to mixing caused by the intensified flow. This effect diminishes when the cavity vibration ceases in case (e). The cases (f) to (h) correspond to the second half of the period where the cavity goes up and the buoyancy effects are enhanced. The flow intensity increases substantially at the beginning of the motion and the recirculation zones remain in the clockwise direction. The flow intensity is then reduced gradually until the cavity stops again in (i) before a new vibration cycle starts. The isotherms are also affected, such that the extent of the hot isotherms is large near the top of the cavity, while the opposite occurs for the colder ones. Moreover, the isotherms exhibit a more horizontal orientation at the center of the cavity, attributed to mixing induced by intensified convective effects.

As for the *Cr* contours, it is important to check where the phase change takes place. Indeed, the purple strips in the *Cr* plots correspond

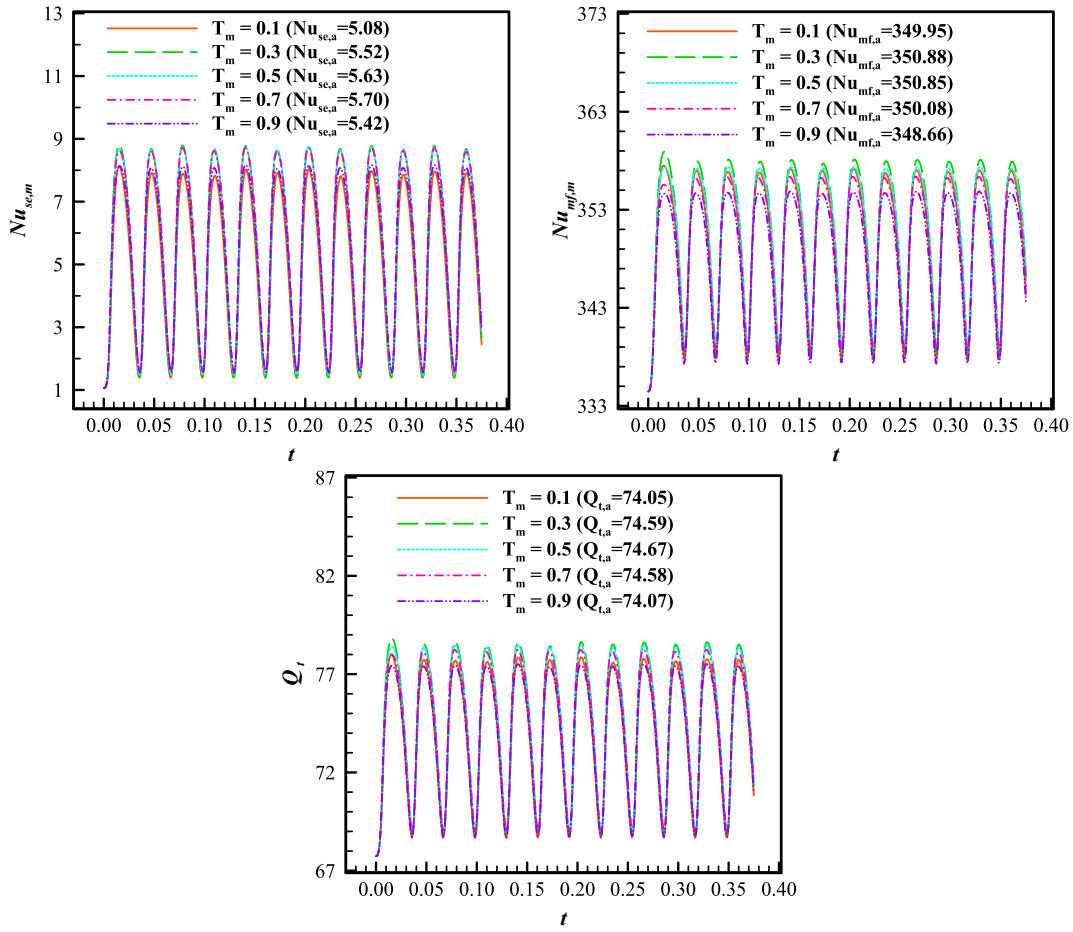

Fig. 15. $Nu_{se,m}$, $Nu_{mf,m}$, and Q_t over the time for different values of T_m.

to regions within the cavity where the core of the NEPCM undergoes a transition from solid to liquid or vice versa. Outside these purple strips, where phase change of the PCM does not occur, the value of *Cr* remains constant at 4 across all cases. The purple ribbon-shaped zones align with the isotherms near the melting temperature, i.e., $T_{mf} = 0.5$. In cases (a) and (i), in the central region of the cavity, the phase change zone extends diagonally from the upper right to the lower left. When the vibration starts and the cavity moves down, flow mixing occurs and the ribbon-shaped zone covers the central part of the enclosure, from the top left to the bottom right. When the chamber moves upwards, a similar shape is observed, but in a different direction, as the ribbon shape extends from the top right to the bottom left. Overall, the external vibration leads to a continuous change in the zone where phase change of the PCM takes place.

Fig. 8 shows the influence of the vibrational Rayleigh number, i.e., Ra_{Ω}, on the isotherms, the flow patterns, and the *Cr* contours. The value of the gravitational Rayleigh number is 10^5, which may not be sufficiently high for the natural convection to dominate. In case (a), when $Ra_{\Omega} = 10^4$, the vibrational effects are weak. The heat transfer through the mixture is primarily governed by the conduction mechanism, as can be seen by the vertical shape of the T_{se} isotherms. The *Cr* contour also shows that phase change is confined to a specific vertical region at the center of the cavity. On the other hand, when Ra_{Ω} is raised to 10^7, the impact of vibration becomes important. The flow intensity is substantially increased, and the isotherms are no longer vertical due to the enhanced mixing. Consequently, the phase change zone becomes larger and covers a greater part of the cavity from its upper left corner to its lower right one.

The time variations of the Nusselt number for the mixture, i.e., $Nu_{se,m}$, the Nusselt number for the metal foam, i.e., $Nu_{mf,m}$, and the overall heat transfer, i.e., Q_t, are plotted in Fig. 9 for different values of the particle concentration, i.e., ϕ. Following the cavity vibration, the two Nusselt numbers also follow a periodic variation around a mean value, which corresponds to the case without vibration. A 12.5% increase in the amplitude of $Nu_{se,m}$ is observed when ϕ is raised from 0 to 0.04. This indicates that the dispersion of nano-sized particles in the host liquid plays a role in heat transfer, either through the absorption or release of heat during the phase change. The impact of ϕ on $Nu_{mf,m}$ is very limited and can be ascribed to the interfacial heat transfer between the liquid and the solid matrix, which in turn can increase when the heat transfer in the mixture is enhanced. In summary, the impact of ϕ on the overall heat exchange is present but limited.

The impact of interfacial heat transfer coefficient, i.e., *h*, on the time variations of $Nu_{se,m}$, $Nu_{mf,m}$, and Q_t is illustrated in Fig. 10. It is clear that higher values of *h* lead to a decrease in the amplitude of $Nu_{se,m}$ and to a rise in the amplitude of $Nu_{mf,m}$. In particular, the amplitude of $Nu_{se,m}$ is almost 7 times higher when *h* is reduced from 5000 to 50, while the amplitude of $Nu_{mf,m}$ is 4 times lower for the same reduction in *h*. Indeed, increasing *h* enhances the interfacial heat exchange between the mixture and the metal foam. More particularly, heat transfers from the solid matrix to the fluid, lowering the temperature of the former and raising the temperature of the latter. Consequently, the temperature gradient in the metal foam is intensified while that of the suspension is weakened. As the thermal conductivity of the metal foam is more than that of the suspension, the overall heat transfer, i.e., Q_t, increases with *h*. In addition, it is noticed that when *h* is augmented from 5000 to 10,000, the change in the $Nu_{mf,a}$ values becomes very small, as for values higher than

5000, the thermal behavior in the chamber approaches the thermal equilibrium between the solid and liquid phases.

Fig. 11 depicts the time variations of Nusselt numbers and Q_t for various vibration frequencies indicated by ξ. Elevating ξ results in a heightened frequency of variation in the two Nusselt numbers but does not affect their amplitude. Indeed, the flow and thermal patterns change due to the external vibration (refer to Figs. 7 and 8). These patterns evolve throughout one oscillation cycle, returning to their initial state upon completion of a full period. Changing the vibration frequency, i.e., the number of vibrations per second, does not affect the variation of patterns during one oscillation as a function of the time step, but it has an impact on the total duration of a cycle that the flow and thermal patterns go back to the initial state and starts varying again. Consequently, the vibrational term affecting buoyancy effects remains consistent in amplitude but varies in frequency. This variability is also reflected in $Nu_{se,m}$ and $Nu_{mf,m}$.

The influence of Stefan number, i.e., *Ste*, on time variations of $Nu_{se,m}$, $Nu_{mf,m}$, and Q_t is shown in Fig. 12. The amplitude of both Nusselt numbers and Q_t increase for lower *Ste*, reaching their maximum values for $Ste = 0.2$. During the decrease of *Ste* from 1 to 0.2, a respective increase of 14% in $Nu_{se,m}$ and 2% in Q_t is observed. Indeed, *Ste* is an indicator of the phase change contribution of NEPCM to the overall heat transfer. A reduction in *Ste* signifies an increased latent heat within the core of the nano-capsules. For lower *Ste* numbers, the contribution of phase change heat exchange is heightened, leading to an overall enhancement of heat exchange within the cavity.

In Fig. 13, time variations of Nusselt numbers and Q_t are plotted for various values of the medium porosity, i.e., ε. As observed, $Nu_{se,m}$ slightly decreases with ε. A 10% reduction in the average of $Nu_{se,m}$ is observed when ε is raised from 0.6 to 0.95. On the other hand, raising ε leads to a substantial increase in $Nu_{mf,m}$. A 15% rise in $Nu_{mf,m}$ is obtained when ε is augmented from 0.6 to 0.95. Indeed, increasing ε leads to expanded void space and a corresponding reduction in the solid matrix volume. This reduction thickens the thermal boundary layer and raises the variations of temperature in the solid matrix. As the effect of ε on $Nu_{mf,m}$ is more important, Q_t also decreases for higher values of ε.

Fig. 14 illustrates the influence of Ra_Ω on the variations of $Nu_{se,m}$, $Nu_{mf,m}$, and Q_t. Increasing Ra_Ω enhances the vibration-induced flow intensity and heat transfer, resulting in higher values for both Nusselt numbers and Q_t. Indeed, Ra_Ω is related to both the convective effects and the amplitude of vibration, such that increasing one of these parameters strongly influences the intensity of the fluid circulation and convection, resulting in a rise of *Nu*. Namely, augmenting Ra_Ω from 10^6 to 10^7 leads to 370%, 5%, and 10% rise in the averages of $Nu_{se,m}$ and $Nu_{mf,m}$, and Q_t, respectively. It is noticed that Ra_Ω affects mostly $Nu_{se,m}$, as the fluid is mainly affected by the cavity vibration.

The impact of the melting temperature of the particle core, i.e., T_m, on the heat transfer in the cavity is shown in Fig. 15. It is clear that T_m has a minimal influence on the heat exchange inside the chamber. A mere 0.1% variation between the maximum and minimum averages of Q_t is found when T_m varies between 0.1 and 0.9. Indeed, altering the phase change temperature of the particle core shifts the locations where melting and solidification take place within the enclosure, aligning with the fluid isotherms, as observed earlier. As the isothermal contours continuously change shape, the core of nano-sized particles undergoes a phase change consistently, regardless of the fusion temperature.

5. Summary and conclusion

The hydrodynamic and thermal behaviors of a mixture comprising nano-sized particles of NEPCM in a differentially heated porous chamber under the effect of external vibrations were analyzed computationally. The heat transfer within the porous medium was modeled using the local thermal non-equilibrium approach. The vibrations are applied in the vertical direction, so they can either enhance or inhibit the gravity effects, depending on the direction of motion. Therefore, the buoyancy-driven natural convection of the NEPCM suspension undergoes both effects during the vibration. The assessment addressed the influence of various parameters tied to nanoparticle properties, porous medium characteristics, and vibration properties on heat transfer within both the suspension and metal foam. It was found that the parameters that have the strongest impact are the vibration Rayleigh number Ra_Ω, the interfacial heat transfer coefficient h between the suspension and metal foam, and the porosity of the medium. The main findings of the present analysis can be summed up as follows:

- Raising Ra_Ω intensifies the vibration-induced fluid motion and enhances mixing and heat transfer, due to high impacts of external vibrations and thermal convection on fluid circulation. Namely, increasing Ra_Ω from 1e6 to 1e7 leads to a 350% rise in the Nusselt number of the suspension $Nu_{se,a}$.
- A reduction in h indicates that the thermal non-equilibrium is more active, and less heat is transferred from the metal foam to the suspension. Namely, the amplitude of $Nu_{se,a}$ can be up to 7 times higher for $h = 100$ compared to $h = 5000$.
- Augmenting the porosity ε diminishes the volume of the solid matrix in the cavity and leads to a reduction in the thermal gradient in the matrix, which is reflected by a decrease in the Nusselt number in the metal foam. For example, increasing ε from 0.6 to 0.95 leads to a 15% reduction in the amplitude of $Nu_{mf,a}$.
- As for the particles, increasing their fraction and altering the phase change temperature results in variations in heat transfer within the porous chamber. Nonetheless, the impact of these parameters remains limited compared to the other parameters. It was found that raising the nanoparticles concentration from 0 to 4% increases the amplitude of $Nu_{mf,a}$ by 12.5%.
- Reducing Stefan number Ste. enhances the contribution of the NEPCM phase change to the total heat transfer. A 14% increase in $Nu_{mf,a}$ was found when Ste. was changed from 1 to 0.2.

These results indicate that the combination of external vibration and NEPCM dispersion can both contribute to changes in flow and heat transfer behavior. These aspects can also be further controlled when the medium in which flow takes place is porous. In the future, considering other geometrical configurations or boundary heating and cooling configurations, as well as the directionality of vibration can be the topic of future research studies. Moreover, designing experiments that can reproduce such behaviors can be beneficial for validation and future implementation.

CRediT authorship contribution statement

Nidhal Ben Khedher: Writing – review & editing, Validation, Software, Resources, Investigation, Data curation. **Hakim S. Sultan Aljibori:** Writing – original draft, Validation, Formal analysis, Conceptualization. **S.A.M. Mehryan:** Visualization, Supervision, Software, Project administration, Methodology, Formal analysis, Conceptualization. **Ahmad Hajjar:** Writing – review & editing, Writing – original draft, Visualization, Resources, Methodology, Investigation. **Mohammad Ghalambaz:** Writing – review & editing, Validation, Supervision, Software, Formal analysis. **Mohamed Boujelbene:** Writing – review & editing, Methodology, Investigation, Conceptualization. **Nasrin B.M. Elbashir:** Writing – review & editing, Investigation, Funding acquisition, Data curation. **Ibrahim Mahariq:** Resources, Supervision, Validation, Writing – review & editing.

Declaration of competing interest

The authors declare that they have no conflict of interest.

Data availability

No data was used for the research described in the article.

Acknowledgment

This study is supported via funding from Prince Sattam bin Abdulaziz University project number (PSAU/2024/R/1445).

Appendix A. Appendix

The fixed parameters are $Pr = 6.2$, $Ra_g = 10^5$, $Da = 10^{-4}$. Furthermore, the numerical simulations have been carried out for the specified set of variables: $Ra_\Omega = 10^3 - 10^7$, $\xi = 5 - 15$, $Ste = 0.2 - 1$, $T_m = 0.05 - 0.95$, $\varepsilon = 0.6 - 0.95$, $h = 10^2 - 10^4$, the volume concentration of NEPCM particles $\phi = 0.0$ and 4%. The default values of parameters in the study are $Ra_\Omega = 10^7$, $\Omega(2\pi\xi) = 100$, $Ste = 0.2$, $T_m = 0.5$, $\varepsilon = 0.8$, $h = 100$, and $\phi = 0.04$. High-porosity metal foam is typically fabricated through electro-deposition and investment casting, exhibiting significant porosity (ranging from 80% to 99%) [43]. Conversely, low-porosity metal foam is produced via infiltration casting, boasting reduced porosity (typically between 60% and 80%), yet showcasing high effective thermal conductivity and a substantial specific area [44]. Moreover, A permeability on the order of 10^{-6} m^2 [45] and an enclosure size on the order of 10^{-2} m can result in $Da = 10^{-4}$.

References

[1] M. Ghalambaz, S.A.M. Mehryan, S.R. Ramezani, A. Hajjar, M. El Kadri, M.S. Islam, O. Younis, M. Ghodrat, Phase change heat transfer in a vertical metal foam-phase change material thermal energy storage heat dissipator, J. Energy Storage 66 (2023) 107370.
[2] M. Ghalambaz, S.A.M. Mehryan, K. Ayoubi Ayoubloo, A. Hajjar, M.S. Islam, O. Younis, M. Ghodrat, Unsteady melting and solidification of a nano-encapsulated phase change materials hybrid nanofluid in an eccentric porous annulus, Waves in Random and Complex Media, 1–27, 2022.
[3] M. Hussain, M. Sheremet, Convective-radiative magnetized dissipative nanofluid (CNTs-water) transport in porous media, using Darcy–Brinkman–Forchheimer model, Int. Commun. Heat Mass Transf. 139 (2022) 106420.
[4] M. Hussain, U. Farooq, M. Sheremet, J. Cui, A.J. Chamkha, Nonsimilar forced convection analysis of magneto nanofluid (CNTs+ Water) flow in Darcy–Forchheimer porous media subjected to thermal radiations and heat generation/absorption, Waves Random Complex Media (2022) 1–14.
[5] N. Gupta, D. Bhargavi, O.D. Makinde, Heat transfer in a MHD couple-stress fluid in a channel filled with porous material: a computational analysis, Int. Commun. Heat Mass Transf. 155 (2024) 107586.
[6] K. Akbarnataj, M.R. Hamidpour, E. Shirani, M.R. Salimpour, Optimization of porous finned heat exchanger configuration using the comprehensive performance methodology, Int. Commun. Heat Mass Transf. 138 (2022) 106318.
[7] T. Tayebi, F. Dahmane, W. Jamshed, A.J. Chamkha, S.M. El Din, Z. Raizah, Double-diffusive magneto-natural convection of nanofluid in an enclosure equipped with a wavy porous cylinder in the local thermal non-equilibrium situation, Case Stud. Thermal Eng. 43 (2023) 102785.
[8] T. Tayebi, Analysis of the local non-equilibria on the heat transfer and entropy generation during thermal natural convection in a non-Darcy porous medium, Int. Commun. Heat Mass Transf. 135 (2022) 106133.
[9] C. Ho, Y.-C. Liu, M. Ghalambaz, W.-M. Yan, Forced convection heat transfer of Nano-Encapsulated Phase Change Material (NEPCM) suspension in a mini-channel heatsink, Int. J. Heat Mass Transf. 155 (2020) 119858.
[10] M.S. Ghoghaei, A. Mahmoudian, O. Mohammadi, M.B. Shafii, H. Jafari Mosleh, M. Zandieh, M.H. Ahmadi, A review on the applications of micro−/nano-encapsulated phase change material slurry in heat transfer and thermal storage systems, J. Therm. Anal. Calorim. 145 (2021) 245–268.
[11] A. Alazzam, N.A. Qasem, A. Aissa, M.S. Abid, K. Guedri, O. Younis, Natural convection characteristics of nano-encapsulated phase change materials in a rectangular wavy enclosure with heating element and under an external magnetic field, J. Energy Storage 57 (2023) 106213.
[12] H. Saleh, R. Muhandaz, A. Irma, I. Fitri, D. Fitraini, A. Sari, H. Nufus, Free convection from a localized heated cylinder with nano encapsulated phase change material and water in a square enclosure, J. Energy Storage 56 (2022) 106028.
[13] M. Ghalambaz, H. Jin, A. Bagheri, O. Younis, D. Wen, Convective flow and heat transfer of Nano-Encapsulated Phase Change Material (NEPCM) dispersions along a vertical surface, Facta Universitatis, Series: Mech. Eng. 20 (3) (2022) 519–538.
[14] N.B. Khedher, S.A.M. Mehryan, A. Hajjar, A.S. Alghawli, M. Ghalambaz, K. A. Ayoubloo, S. Dhahbi, Optimizing heat flow: Nano-encapsulated phase change materials in vibration-enhanced gravity-driven thermal convection, Int. Commun. Heat Mass Transf. 151 (2024) 107212.
[15] A. Tahmasebi, H. Zargartalebi, S. Mehryan, M. Ghalambaz, Thermal and hydrodynamic behavior of suspensions comprising nano-encapsulated phase change materials in a porous enclosure, Int. Commun. Heat Mass Transf. 116 (2020) 104634.
[16] K. Guedri, F. Riaz, B.M. Fadhl, M.K. Agrawal, N.A. Shah, B.M. Makhdoum, H. M. Youshanlouei, Use of nano-encapsulated phase change material mixed with water for natural convection cooling in combination with nickel foam, Thermal Sci. Eng. Progr. 42 (2023) 101934.
[17] F.C. Wang, Effects of vibration (G-jitters) on convection in micro-gravity, Alabama Univ., Research Reports: 1994 NASA (ASEE Summer Faculty Fellowship Program), 1994.
[18] N.K. Murad, H.D. Lafta, S. Elis Abdullah, The effect of transverse vibration on the natural convection heat transfer in a rectangular enclosure, Int. J. Mech. Eng. Technol. 10 (6) (2019).
[19] S. Biringen, G. Danabasoglu, Computation of convective flow with gravity modulation in rectangular cavities, J. Thermophys. Heat Transf. 4 (3) (1990) 357–365.
[20] D. Li, X. Yang, S. Wang, D. Duan, Z. Wan, G. Xia, W. Liu, Experimental research on vibration-enhanced heat transfer of fin-tube vehicle radiator, Appl. Therm. Eng. 180 (2020) 115836.
[21] N. Joshy, M. Hajiyan, A.R.M. Siddique, S. Tasnim, H. Simha, S. Mahmud, Experimental investigation of the effect of vibration on phase change material (PCM) based battery thermal management system, J. Power Sources 450 (2020) 227717.
[22] A. Dawood, B. Manocha, S. Ali, The effect of vertical vibrations on natural convection heat transfer from a horizontal cylinder, Int. J. Heat Mass Transf. 24 (3) (1981) 491–496.
[23] S.K. Mishra, A. Tripure, A. Mishra, P. Singh, Effects of vibrational flow on nanofluid flow behavior under different temperature boundary conditions, Numer. Heat Transf. A Appl. (2024) 1–17.
[24] B.K. Khudhair, A.M. Saleh, A.L. Ekaid, An experimental study of forced vibration on natural convection between closed ended concentric and eccentric annular of horizontal cylinder, Diagnostyka 24 (2) (2023).
[25] A. Medelfef, D. Henry, S. Kaddeche, F. Mokhtari, S. Bouarab, V. Botton, A. Bouabdallah, Linear stability of natural convection in a differentially heated shallow cavity submitted to high-frequency horizontal vibrations, Phys. Fluids 35 (8) (2023).
[26] B.K. Khudhair, A.M. Salh, A. Ekaid, Vibration effect on natural convection heat transfer in an Inclosed cubic cavity, in: IOP Conference Series: Materials Science and Engineering, IOP Publishing, 2021, p. 012060.
[27] H. Kimoto, H. Ishida, Vibration effects on the average heat transfer characteristics of the natural convection field in a square enclosure, Heat Transf. Asian Res. Co-sponsored by the Soc. Chem. Eng. Japan Heat Transf. Div. ASME 29 (7) (2000) 545–558.
[28] B.S. Rao, S. Ravi Babu, Experimental investigation on natural convection heat transfer augmentation with vibration effect, Int. Res. J. Eng. Technol. 6 (8) (2019).
[29] E.-H. Zidi, A. Hasseine, N. Moummi, The effect of vertical vibrations on heat and mass transfers through natural convection in partially porous cavity, Arab. J. Sci. Eng. 43 (2018) 2195–2204.
[30] P. Nag, A. Bhattacharya, Effect of vibration on natural convection heat transfer from vertical fin arrays, Lett. Heat Mass Transf. 9 (6) (1982) 487–498.
[31] A.I. Alsabery, A.S. Abosinnee, M.A. Ismael, A.J. Chamkha, I. Hashim, Natural convection inside nanofluid superposed wavy porous layers using LTNE model, Waves Random Complex Media (2021) 1–29.
[32] D.A. Nield, A. Bejan, Convection in Porous Media, 5th ed., Springer, 2017.
[33] S. Barlak, O.N. Sara, A. Karaipekli, S. Yapıcı, Thermal conductivity and viscosity of nanofluids having nanoencapsulated phase change material, Nanoscale Microscale Thermophys. Eng. 20 (2) (2016) 85–96.
[34] J.-W. Wu, W.-F. Sung, H.-S. Chu, Thermal conductivity of polyurethane foams, Int. J. Heat Mass Transf. 42 (12) (1999) 2211–2217.
[35] N. García-Acosta, P. Salgado Sánchez, J. Jiménez, Ú. Martínez, J.M. Ezquerro, Thermocapillary-enhanced melting of different phase-change materials in microgravity, Microgravity Sci. Technol. 34 (5) (2022) 92.
[36] W.-S. Fu, W.-J. Shieh, Transient thermal convection in an enclosure induced simultaneously by gravity and vibration, Int. J. Heat Mass Transf. 36 (2) (1993) 437–452.
[37] S.A.M. Mehryan, P. Goudarzi, Seyed M. Hashem, M. Zadeh, O. Ghodrat, M. Ghalambaz Younis, Thermal vibrational and gravitational analysis of a hybrid aqueous suspension comprising ag–MgO hybrid nano-additives, Int. Commun. Heat Mass Transf. 126 (2021) 105345.
[38] M. Ghalambaz, S.M. Hashem Zadeh, S.A.M. Mehryan, A. Haghparast, H. Zargartalebi, Free convection of a suspension containing nano-encapsulated

phase change material in a porous cavity; local thermal non-equilibrium model, Heliyon 6 (5) (2020) e03823.
[39] A.C. Baytas, I. Pop, Free convection in a square porous cavity using a thermal nonequilibrium model, Int. J. Therm. Sci. 41 (9) (2002) 861–870.
[40] B. Calcagni, F. Marsili, M. Paroncini, Natural convective heat transfer in square enclosures heated from below, Appl. Therm. Eng. 25 (16) (2005) 2522–2531.
[41] M. Ghalambaz, A.J. Chamkha, D. Wen, Natural convective flow and heat transfer of Nano-Encapsulated Phase Change Materials (NEPCMs) in a cavity, Int. J. Heat Mass Transf. 138 (2019) 738–749.
[42] H. Saleh, Z. Siri, M. Ghalambaz, Natural convection from a bottom heated of an asymmetrical U-shaped enclosure with nano-encapsulated phase change material, J. Energy Storage 38 (2021) 102538.
[43] P.-S. Liu, Introduction to Porous Materials, Tsinghua University Press, 2004, p. 299.
[44] X. Hu, F. Zhu, X. Gong, Experimental and numerical study on the thermal behavior of phase change material infiltrated in low porosity metal foam, J. Energy Storage 26 (2019) 101005.
[45] A. Bhattacharya, V.V. Calmidi, R.L. Mahajan, Thermophysical properties of high porosity metal foams, Int. J. Heat Mass Transf. 45 (5) (2002) 1017–1031.